





# Design of a sparse irregular array for beyond 5G base stations

by

M. Buenaventura Camps

to obtain the degree of Master of Science  
at the Delft University of Technology,  
to be defended publicly on Thursday July 8, 2021 at 9:00 AM.

Student number: 5129745  
Project duration: October 1, 2020 – July 8, 2021  
Thesis committee: Prof. DSc. A. Yarovoy, TU Delft, supervisor  
Dr. ir. M. Alavi, TU Delft  
Dr. P. Freidl, NXP Semiconductors  
Dr. ir. Y. Aslan, TU Delft, daily supervisor

*This thesis is confidential and cannot be made public until July 8, 2023.*

An electronic version of this thesis is available at <http://repository.tudelft.nl/>.



## Abstract

New generations of mobile communications are much more demanding in order to provide critical real-time services and extremely fast connections that have become feasible with 5G. A wider spectrum is needed to achieve such high data rates and millimeter-wave frequencies are used for this purpose. Adaptive beamforming is applied at base stations through active phased antenna arrays to shape and steer the beams at each user, so coverage distance is extended and resource sharing among users is more efficient.

Different approaches to the design of active phased arrays for mm-wave base stations to realize the "one beam per user" concept are analyzed and compared. Particular attention to mutual interference between the beams is given. A novel aperiodic, uniformly-fed, active integrated antenna array design is presented as an appealing alternative to minimize user inference based on a multi-disciplinary array synthesis approach. Implementation challenges of such aperiodic array are investigated and the performance is compared to those of a periodic array. The complete design and its simulation results show an interference reduction around 6 dB and similar gain as compared to the regular array taken as reference.



## Acknowledgements

This master thesis would not have been possible without the support and encouragement of Philipp and Yanki. I would like to thank them both for their excellent guidance during this year. I would also like to thank Alexander Yarovoy and Marcel Geurts, without whose supervision and cooperation I would not have been able to go through this project.

My family's trust and support during all my studies, even in the lowest moments have encouraged me to continue pursuing my goals. To my dearest friends from Spain and the new ones I had the pleasure to meet along the way, thanks for always finding the way to cheer me up and make my days better. With his endless advice and inspiration, Marc Vizcarro has always been there for helping me taking the best decision at each moment. A special mention to Carlos Ruiz, for being a great companion during these two years. And of course Alex, I cannot thank you enough for always being there.

This work was supported in part by the Netherlands Organisation for Scientific Research, and in part by NXP Semiconductors in the framework of the partnership program on Advanced 5G Solutions within the project number 15590 entitled "Antenna Topologies, and Front-end Configurations for Multiple Beam Generation".



# Contents

|          |   |           |
|----------|---|-----------|
| <b>1</b> | <b>Introduction</b>   | <b>1</b>  |
| 1.1      | Motivation . . . . .  | 1         |
| 1.2      | Literature review . . . . .   | 2         |
| 1.2.1    | Introduction to 5G and beyond . . . . .                               | 2         |
| 1.2.2    | An unconventional approach: aperiodic mm-wave phased arrays . . . . . | 4         |
| 1.2.3    | Antenna integration for silicon-based mm-wave phased arrays . . . . . | 5         |
| 1.3      | Research approach . . . . .   | 8         |
| 1.4      | Novelties . . . . .   | 9         |
| 1.5      | Outline of the thesis . . . . .                                       | 10        |
| <b>2</b> | <b>Optimum sparse array topology selection</b>                        | <b>11</b> |
| 2.1      | Antenna specifications . . . . .                                      | 11        |
| 2.2      | Criteria . . . . .  | 12        |
| 2.3      | Analysis and comparison . . . . .                                     | 13        |
| 2.4      | Conclusions . . . . .   | 16        |
| <b>3</b> | <b>Design of aperiodic phased array</b>                               | <b>17</b> |
| 3.1      | Board technology . . . . .  | 17        |
| 3.2      | Antenna block . . . . .   | 18        |
| 3.2.1    | Single element . . . . .  | 18        |
| 3.2.2    | Antenna array . . . . .   | 19        |
| 3.3      | Feeding network . . . . .   | 20        |
| 3.4      | Distribution network . . . . .  | 21        |
| 3.5      | Control signals . . . . .   | 22        |
| 3.6      | Supply network . . . . .  | 23        |
| 3.7      | Panel design . . . . .  | 24        |
| 3.8      | Recommended improvements . . . . .                                    | 26        |
| 3.8.1    | Dual-polarization array layout optimization . . . . .                 | 26        |
| 3.8.2    | Sequential rotation of the antenna elements . . . . .                 | 27        |
| 3.9      | Conclusions . . . . .   | 30        |
| <b>4</b> | <b>Analysis of losses</b>   | <b>31</b> |
| 4.1      | Feeding network . . . . .   | 32        |
| 4.2      | Distribution network . . . . .  | 33        |

---

|          |   |           |
|----------|---|-----------|
| 4.3      | Calibration approach . . . . .            | 35        |
| 4.4      | Conclusions . . . . .                     | 36        |
| <b>5</b> | <b>Aperiodic antenna array analysis</b>   | <b>37</b> |
| 5.1      | Resonance and S-Parameters . . . . .      | 37        |
| 5.2      | Beamforming results . . . . .             | 37        |
| 5.3      | Embedded element pattern . . . . .        | 41        |
| 5.4      | Comparison with a regular array . . . . . | 42        |
| 5.5      | Conclusions . . . . .                     | 46        |
| <b>6</b> | <b>Conclusions and future work</b>        | <b>47</b> |
| 6.1      | Conclusions . . . . .                     | 47        |
| 6.2      | Future work . . . . .                     | 49        |
| 6.3      | Publications . . . . .                    | 49        |
| <b>A</b> | <b>Panel layout</b>                       | <b>55</b> |
| <b>B</b> | <b>Test board layout</b>                  | <b>63</b> |

# Chapter 1

## Introduction

### 1.1 Motivation

The base station antenna systems for 5G and beyond ultimately aim to achieve the “one-beam-per-user” concept, with a large number of flexible simultaneous co-frequency beams at millimeter-wave bands where the spectrum is available for wide bandwidth. In such multi-user communication systems, it is crucial to suppress the inter-beam interference sufficiently so as to achieve high spectral efficiency and service quality.

The current state-of-the-art arrays for 5G base stations are chip-integrated active mm-wave phased arrays based on regular dense and completely symmetrical structures of the antenna element placements. Many benefits are well-known from this type of structure since it allows an easy design, uncomplicated manufacturing, and stable performance even under no calibration. However, it has important drawbacks when implemented on the next generation mm-wave base stations. Due to the periodicity of the structure, the high interference that may originate from the first sidelobe is too high to achieve high spectral density and quality of service, particularly when multiple users are relatively close to each other. On the other hand, the high density of elements on the antenna aperture leads to thermal issues that can deteriorate the performance and safety of the system.

Therefore, aperiodic arrays are a promising alternative to address the interference issues of mm-wave base stations. Breaking the periodicity by placing the antenna elements in a non-regular grid, the maximum sidelobe level can be drastically reduced. From a theoretical point of view, aperiodic sparse arrays have been proposed in [1] as an effective solution to address such interdisciplinary problems simultaneously, yet the design challenges due to the large layout irregularity still need to be addressed to realize such arrays. By overcoming the design challenges, this project aims at having a fully aperiodic or quasi-modular chip-integrated active array operational. Besides the selection of the optimum topology from a performance and design feasibility point of view, the design of the feeding network, routing of the beamforming ICs, calibration, and experimental verification are within the scope of the thesis.

## 1.2 Literature review

### 1.2.1 Introduction to 5G and beyond

The last generations of mobile communications were mainly focused on operating in wider spectrum ranges, offering higher data rates and better traffic handling capabilities. These are still key factors for next-generations, where a very wide range of frequency bands are available due to the release of millimeter-wave frequencies [2]. Furthermore, 5G has also other goals that differentiate this generation from all the previous ones. Its potential is expanded much further due to the integration of massive IoT support, the support for critical services, and the modifications of the core network functionality such that distributed cloud computation is improved [3]. The sixth-generation goes even further with the introduction of AI, considering machines as main users, using an open-source software and the contribution for achieving social goals is increased [4].

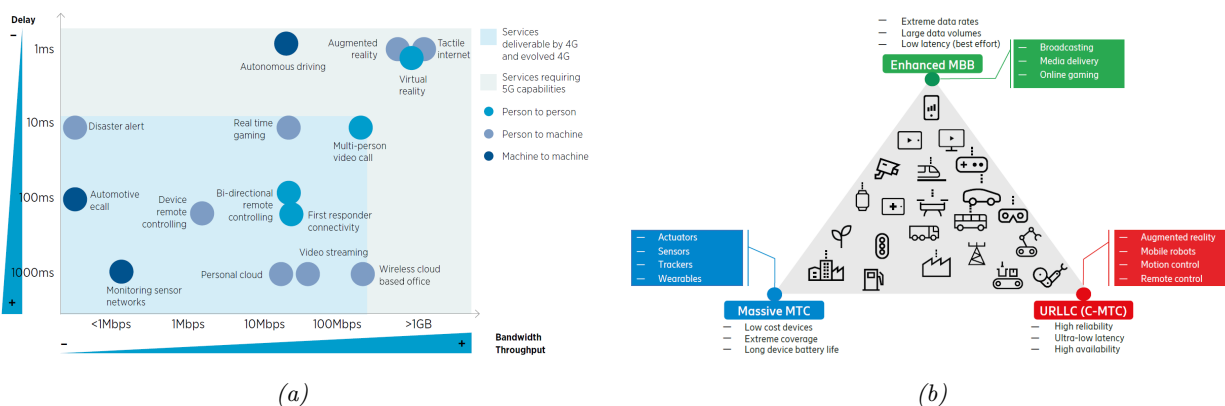


Figure 1.1: Capabilities and applications of 5G: (a) Bandwidth and latency requirements of potential 5G use cases [5] and (b) diagram of 5G capabilities [3]

Therefore, the fifth-generation of wireless communications is defined from two points of view according to [6]. From the hyper-connected view, it is seen as a combination of already existing systems (2G, 3G, 4G, WiFi, and others) in order to allow higher coverage, availability and, particularly, higher network density as a key differentiator for enabling Machine-to-Machine (M2M) services and the Internet of Things (IoT). On the other hand, seen from a more traditional view, it is the next-generation radio access technology with specific data rates and latency targets. From both definitions, the requirements for 5G are listed as follows [6]:

- 1-10Gbps connections to end points in the field (i.e. not theoretical maximum)
- 1 millisecond end-to-end round trip delay (latency)
- 1000x bandwidth per unit area
- 10-100x number of connected devices
- (Perception of) 99.999% availability
- (Perception of) 100% coverage
- 90% reduction in network energy usage

- Up to ten year battery life for low power, machine-type devices

Although the eight requirements are important for specific applications, only two of them are generation-defining attributes so that would be unique to 5G: sub-1ms latency and >1Gbps downlink speed. Satisfying these two requirements, new use cases become feasible with 5G that was not with previous technology. As shown in Figure 1.1a, critical real-time services like autonomous driving can be enabled with the ultra-low latency offered by the new generation, or applications that require extreme fast connectivity such as augmented reality. The representative categories of 5G are shown in Figure 1.1b, which will continue to improve moving towards 6G [4].

The spectrum allocated for 5G can be divided into 3 different bands: sub-1GHz, allows good coverage and is very useful for wide-area IoT use cases; 1GHz to 6GHz, offers a good trade-off of coverage and capacity; and bands above 6GHz (mmWave range, e.g. 26GHz, 28GHz and 40GHz) provides high capacity communication within short range, which emerge as key for achieving the 5G ultra-high speed [5].

Due to the limited cell radius at mm-wave bands, the widespread coverage using the traditional network topology would suppose a huge increase of base station deployments. For this reason, beamforming is widely used to extend the cell radius by focusing the signal energy into a narrow beam aiming at the connected end-user device, as in Figure 1.2, instead of broadcasting the signal used in previous generations.

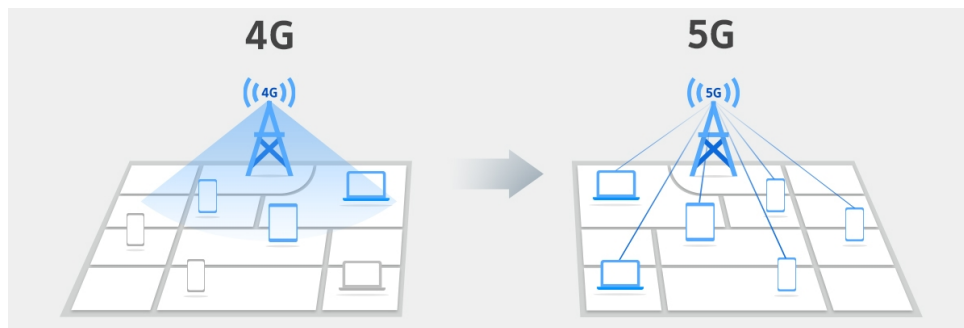


Figure 1.2: Coverage strategy of base stations in 4G and 5G [7]

In addition, the high-speed communications targeted require a wide frequency band. However, the spectral resources are limited and have to be shared with the near devices. Taking advantage of the narrow beams generated at the base stations, the resources can be shared through spatial multiplexing, which allows for a higher capacity in terms of terminals. Massive MIMO (Multiple-Input, Multiple-Output) is the perfect approach to increase the bandwidth of each device while increasing capacity and cell range. Therefore, multiple simultaneous narrow beams should be created at the base station using co-frequency bands, named SDMA (Spatial Division Multiple Access). The beams must have sufficient high gain for good coverage and low inter-beam interference [6] [8] [1].

Base stations of next generations need sufficient simultaneous frequency re-use through the formation of multiple beams (SDMA) with high gain for good coverage and low inter-beam interference, hence low maximum sidelobe level. However, the active phased antenna arrays that form and steer the beams in a massive MIMO scenario also create radio interference issues among downlinks that have to be mitigated.

Uniformly-fed (with optimal power efficiency) regular layout arrays with  $0.5\lambda$  element spacing offers a maximum sidelobe level (SLL) of about -13 dB which corresponds to the first sidelobe. In some statistical studies, where the individual user metrics are not the main concern, the parameter of interest is the average SLL [9]. However, the maximum SLL is very important to guarantee high quality of service and fairness among all the users, part of who might suffer from the high sidelobes otherwise [10].

In some cases, smart user selection strategies are used to avoid high interference but that increases complexity in Media Access Control (MAC) layer and might be more biased as compared to random user selection with some angular user separation constraint. This separation should be larger than the beamwidth of the base station array to resolve the users with low-interference and high-gain beams [11]. Moreover, in the case of uniformly-fed periodic arrays, the separation should be large enough to avoid the first sidelobe if it is desired to ensure high quality of service for all users. Such a constraint seriously limits the frequency reuse and creates blind regions in the coverage [12]. If the maximum SLL is minimized while keeping a similar or improved beam resolution, system optimality can be achieved.

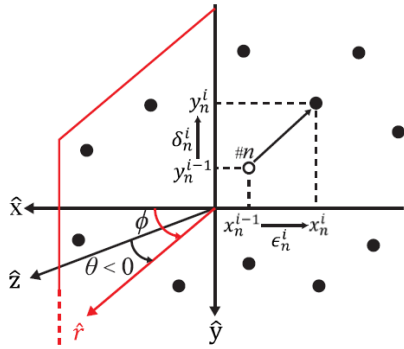
Amplitude tapering is usually applied for sidelobe level reduction but the power received by the user is significantly degraded and the beamwidth becomes larger, which limits the frequency reuse. There are also zero-forcing based nulling strategies (based on phase tapering and only slight amplitude variations across the array with proper beam separation constraints) which are decent in terms of power tapering but the processing complexity gets very large with the number of elements and users due to the matrix inversion involved. Besides, the nulls are very sensitive the channel impurities and system imperfections [11]. Therefore, a new approach is needed in order to address this issue.

### 1.2.2 An unconventional approach: aperiodic mm-wave phased arrays

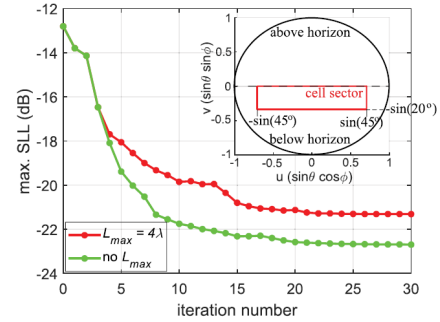
The inter-disciplinary (including electromagnetics, signal processing, radio resource management) system discussions given above clearly show that there is a growing demand for power-efficient, low sidelobe phased arrays in the next-generation base stations for multi-user communications. In the recent literature, it has been shown that uniformly-fed, use-case optimized, aperiodic phased array concept has, in theory, great potential in addressing these issues [13]. However, the implementation challenges and performance trade-offs of such aperiodic arrays in a beamformer chip integrated, active phased array module has not yet been investigated.

This appealing approach is a position-only control technique (Fig. 1.3a) presented in [14] that can be used to introduce irregularity in the array layout, keeping a progressive phase shift at the uniform-amplitude elements while achieving optimal power efficiency. The topology is optimized such that the maximum SLL is minimized within the visible space for a beam scanned freely inside a pre-given cell sector (Fig. 1.3b).

Other works present algorithms with similar goals and approaches, but none of them are created for and compatible with the requirements of SDMA for 5G. The selected one highlights from the others also due to the multibeam optimization (needed for SDMA), offers the simplicity of exciting the elements with uniform amplitude and a minimum inter-element spacing is respected to avoid high mutual coupling and thermal issues.



(a) Scheme of position-only technique [14]



(b) Convergence of SLL minimization [14]

Figure 1.3: Position-only technique to minimize SLL: (a) scheme and (b) convergence of SLL minimization [14]

### 1.2.3 Antenna integration for silicon-based mm-wave phased arrays

In order to enable beamforming and beam steering, silicon-based phased arrays are commonly used in mm-wave for their ability to create complex electromagnetic interference radiation patterns in space. Its technology using innovative RFIC and packaging solutions are one key factor to set them as cost-effective and power efficient at the mm-wave frequency range. Moreover, a relatively large number of antenna elements are needed to extend the distance coverage at base stations. For this reason, multiple Si-based ICs are commonly used in a modular fashion to control the antenna elements. Therefore, phased array scaling is a key factor to achieve the desired link margin [15].

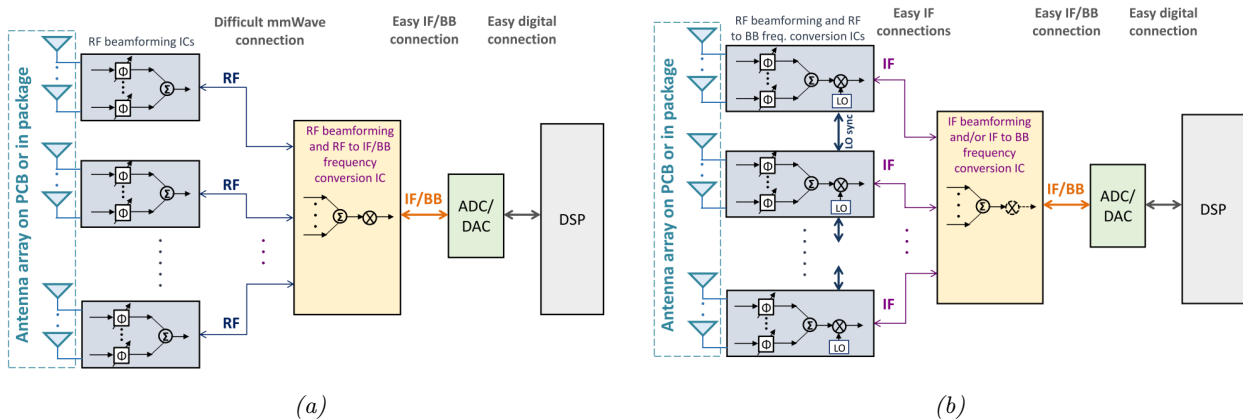


Figure 1.4: Beamforming architectures for silicon-based phased arrays (a) RF beamforming and (b) RF/IF combination beamforming [15]

Different beamforming options are possible based on which frequency or stage the beamforming is applied. The most common are beamforming in RF, local oscillator (LO), intermediate frequency (IF), or digital beamforming. While digital beamforming is an attractive approach since it can create simultaneous beams, it becomes too expensive at high frequencies (FR2 and FR3), with a large number of antenna elements and large bandwidth. In those cases, RF beamforming (Fig. 1.4a) or a

combination of RF/IF beamforming (Fig. 1.4b) is preferred. Both of them have different functions that are usually managed by different kinds of ICs: RF phase shifting, RF combining/splitting, frequency conversion, analog-to-digital conversion, and digital signal processing. Although RF beamforming simplifies the system design with less circuitry, the mm-wave signals in the package need to be routed from beamforming IC to frequency conversion IC. This can become a challenge and more expensive substrates are needed.

Regardless of the beamforming architecture in use, Si-based phased arrays at mm-wave frequencies require a tight antenna integration solution due to the spacing among antenna elements (often half-wavelength of carrier frequency) [15]. Besides the losses on the propagation path, losses are also larger in the interconnections so integrate antennas with IC is a good solution to minimize them [16]. The two major implementation approaches for array design are antenna on PCB and Antenna in package (AiP). The first one allows the lowest cost, setting the RFICs on the board side opposite to the radiation direction. The latter places antennas on the first level of the package and the module can be attached to a second level PCB in order to create a larger array [15]. An example can be seen in Figure 1.5, where the antenna module is homogeneously embedded within the 12-layer carrier board, enabling simplified, monolithic fabrication and assembly [17].

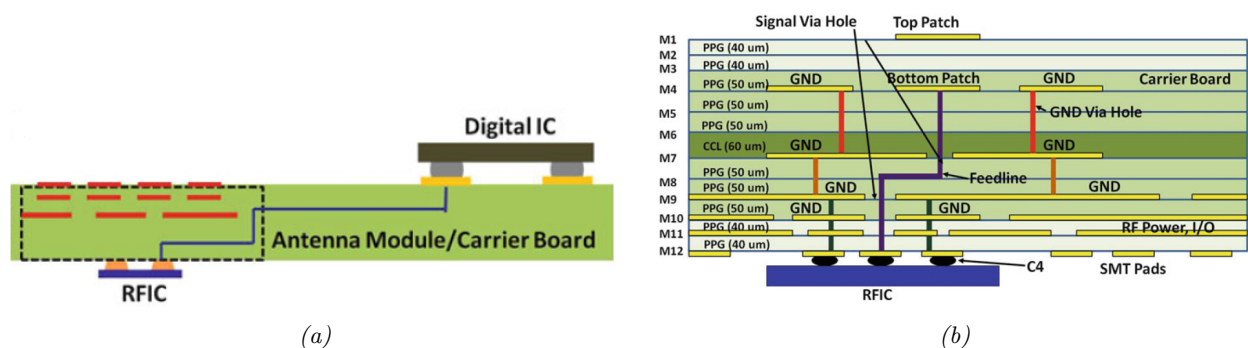


Figure 1.5: Layer configuration for chip-integrated antenna (a) simplified [17] and (b) detailed PCB stack [18]

The substrate material and process selected for the antenna packaging are key to integrate antennas and RFIC successfully. A wide range of substrate technology variety includes low-temperature co-fired ceramic (LTCC) and multi-layer organic laminate, among others [15]. For mm-wave antennas to operate at the base stations of the next-generation network communication, the organizations prefer a single multi-layered RF board antenna with low-cost and low-profile [14].

However, the main key for Si-based phased arrays remains on the co-design and optimization of the antenna element to achieve targeted specifications (gain, bandwidth, radiation pattern) taking into account the rest of the elements of the PCB or package:

- Substrate material properties and manufacturing process
- System and circuitry requirements
- Interconnect flexibility
- Thermo-mechanical compatibility

- IC assembly
- Board integration constraints

Although several antenna structures are easy to integrate to PCB or AiP (slot, grid, Yagi antennas, etc.), aperture coupled or probe-fed patch antenna are the preferred option since the antenna ground plane separates and decouples antenna radiators from feed lines, so they can be optimized independently. This introduces a very important advantage because antenna co-design is then also not needed for routing other low-frequency signals and passive components [15].

Another important factor that must be taken into account, is that front-end calibration should be avoided or simplified by equalizing the length of the feed lines or reducing the gain variation. Although phase and gain control are available, the calibration process can become too complex [15].

As already mentioned in the motivation, the current work on 5G base station antenna arrays is based on regular dense and completely symmetrical structures since it allows an easy design, uncomplicated manufacturing and stable performance even under no calibration [19]. In Table 1.1 some examples of state-of-the-art active integrated mm-wave phased arrays (Figure 1.6) and their performance based on measurements are listed. All of them have a regular dense structure with 64 or 256 elements. While the Effective Isotropic Radiated Power (EIRP) at broadside in all cases is around 55 dBm for small cell deployment [23], the maximum SLL goes up to -10 dB for the

*Table 1.1: A performance comparison of several state-of-the-art active phased array antenna systems*

| Array  | UCSD [19]                                 | IBM [20]                                     | Nokia Bell Labs [21]                            | Qualcomm [22]   | NXP/TNO (taken as reference)                 |
|--|---|--|---|---|--|
| Number of elements                               | 8x8                                       | 10x10 with two outer rings of dummy elements | 8x8   | 8x32 with two rows and four columns of dummy elements | 10x10 with two outer rings of dummy elements |
| Transmit/receive beamformer chips                | 16  | 4  | 16  | 32  | 16   |
| Central frequency (GHz)                          | 30  | 28   | 28  | 28  | 26   |
| Antenna element type                             | Stacked patch antennas                    | Aperture coupled patch                       | Capacitively coupled patch                      | Patch antennas  | Stacked patch antennas                       |
| Antenna array layout                             | Square grid $0.5\lambda$ by $0.63\lambda$ | Square grid $0.5\lambda$ spaced              | Equilateral triangular grid $0.5\lambda$ spaced | Square grid total active aperture of 160mm by 40mm    | Square grid $0.5\lambda$ spaced              |
| Polarization                                     | Single                                    | Dual   | Single  | Dual  | Dual   |
| EIRP (dBm) at broadside                          | 52  | 54   | 48  | 64  | 56   |
| Max. SLL (dB) for a beam at broadside            | -12                                       | -13  | -13   | -10   | -12  |
| Max. SLL (dB) for a beam at EoC                  | -10                                       | -10  | -10   | -8  | -10  |
| Reference scan range (deg.) in elevation/azimuth | $\pm 25 / \pm 50$                         | $\pm 50 / \pm 50$                            | $\pm 45 / \pm 45$                               | $\pm 50 / \pm 50$                                     | $\pm 45 / \pm 45$                            |

broadside beam and -8 dB for a beam scanned to the edge-of-coverage (EoC).

As seen in Table 1.1, these arrays have important interference drawbacks when implemented on the next generation mm-wave base stations. The periodicity of the structure leads to the appearance of a first sidelobe which is too high to address the isolation requirements among users. Additionally, the high density of elements on the antenna aperture causes thermal issues that can deteriorate the performance and safety of the system. The overheating can be relaxed by using a relatively large inter-element spacing that would create more surface area around the chips that act as hotspots, which might increase the level of side lobes and lead to the formation of undesired grating lobes if it is not dealt with. Therefore, there is a trade-off between the interference cancellation and the cooling capacity of the array from the layout sparsity point-of-view [24].

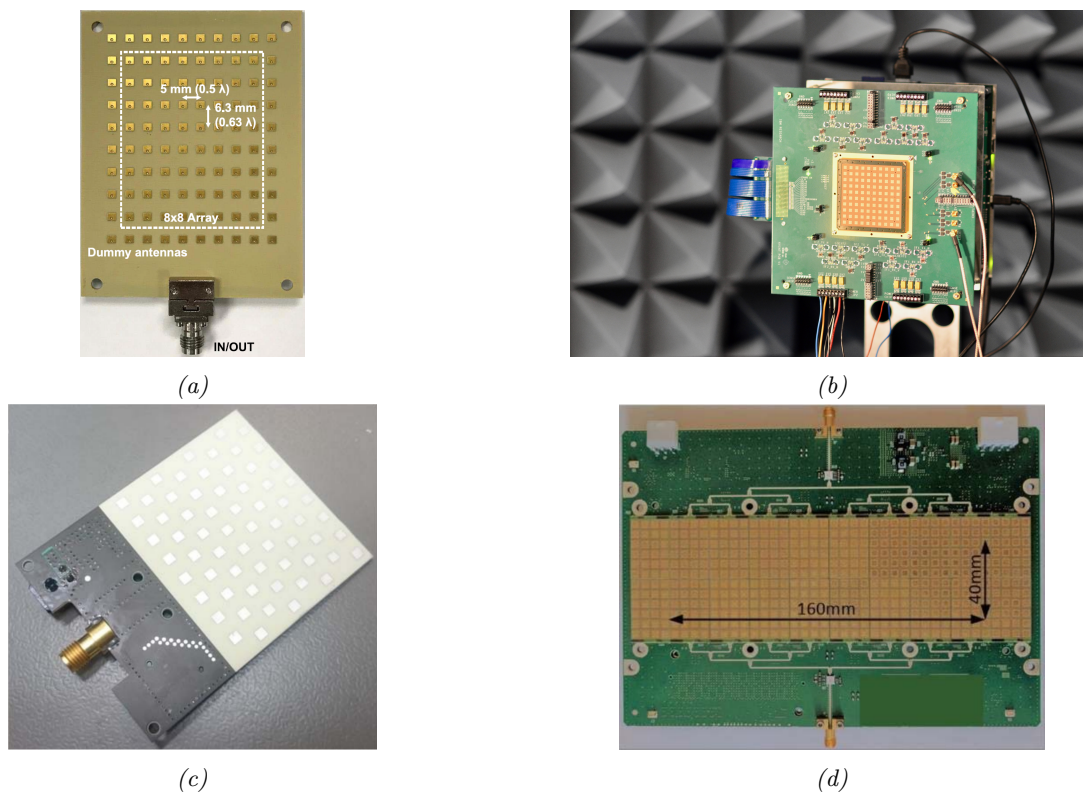


Figure 1.6: 5G state-of-the-art active integrated phased base station antenna arrays from the industry. (a) UCSD [19] (b) IBM [20] (c) Nokia Bell Labs [21] (d) Qualcomm [22].

### 1.3 Research approach

In order to realize an antenna solution that could address the thermal issues and high interference of the next generation mm-wave base stations, the new topologies of sparse irregular arrays are generated with the algorithm proposed in [1] so it is designed from an interdisciplinary point of view. The performance of the prototype will be finally compared with a demo antenna to demonstrate the performance improvement, especially in terms of EIRP and SLL. For the sake of comparison, the new sparse array should be as similar as possible to the reference prototype. The reference regular

antenna is a 10x10 array with 8x8 active elements at the center and two outer rings of dummy elements of patch antennas as shown in Figure 1.7.

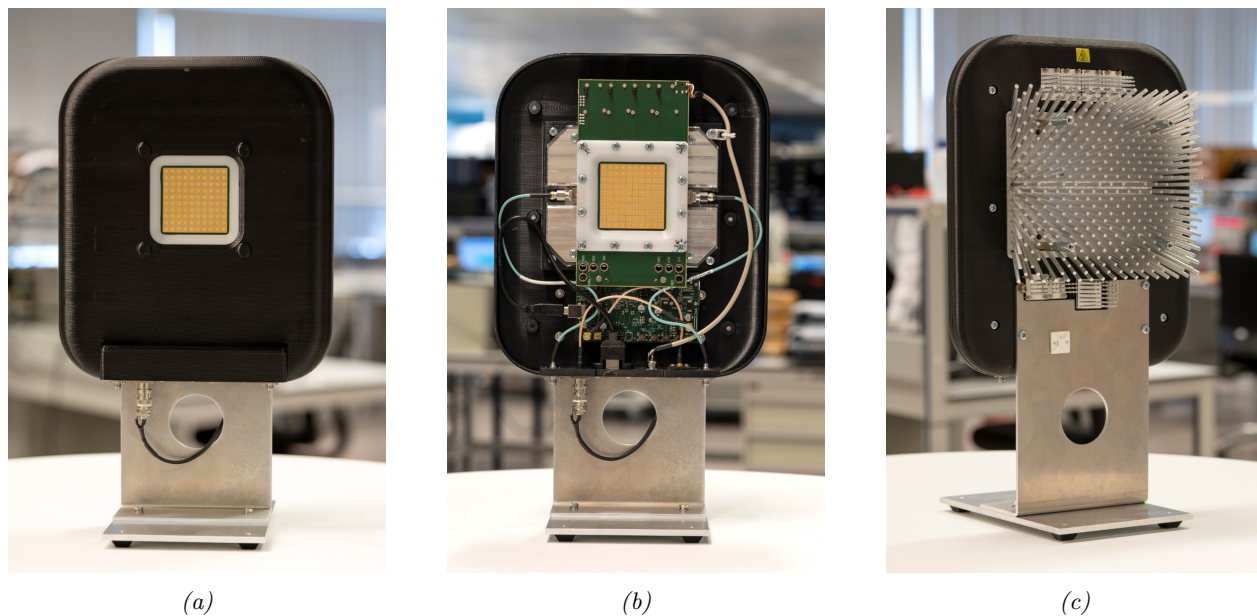


Figure 1.7: The active phased array with a regular square-grid layout used as reference (in courtesy of NXP/TNO) from (a) front view closed, (b) open and (c) back view

First of all, a complete specification of the sparse antenna panel should be established as a starting point for the antenna design. Then, a feasibility study should take place in order to select the optimum array topology under the criteria of both performance array and routing length from beamforming IC to the antenna element. The latter criterion is key to reduce losses after the power amplifier, critical for scanning performance. The antenna elements should be clustered and connected to the beamforming IC in a way that the loss is minimized and the difference between line lengths is allowable for a good performance.

Once the topology and placement of ICs are determined, the layout of the feeding network should be designed by using as much as possible from the antenna demo for a fair comparison. Besides the antenna panel, test structures should also be created in order to make a complete test of the different building blocks. Once the design of the aperiodic antenna array system is available, the analysis of losses and validation is done through full-wave simulations. After positive results from both loss and array validation, the panel and test board structures should be manufactured for their experimental verification. A proper calibration approach and a set of measurements will be carried out in order to test and validate the performance experimentally. Finally, the differences between the results from measurements and simulations will be reported.

## 1.4 Novelties

In this thesis, important novel aspects have been studied, developed, and analyzed related to aperiodic phased arrays. The novelties of this work are highlighted and listed as follows:

- A first-time design of an irregular feeding network with multi-channel mm-wave beamforming chips is accomplished.
- A novel design constraints on chip placement and line length equalization for calibration simplification is proposed.
- In addition, a complete design of an aperiodic antenna array system has been also done, including sub-systems such as control unit, power unit, or cooling unit.
- A comparison of losses for regular and irregular networks under practical design is performed for the first time.
- Finally, a novel investigation of irregularly-placed element mirroring has been done on the idealized radiation patterns obtained from the optimizers.

## 1.5 Outline of the thesis

The document of the thesis is structured as follows. Firstly, an introductory section explains the motivation behind this project based on the current state-of-the-art antenna arrays for 5G base stations, followed by the approach of the conducted research and technical work together with the value of the presented novelties.

The feasibility study of the research is presented in the second chapter. The goal of the feasibility study is to select the optimum array layout most suitable regarding the requirements set for the antenna. The criteria for the selection are explained in detail and from the comparison among the proposed layouts, the best array structure is selected for the following design based on the criteria and considering the targeted specifications.

Moving on to the third chapter, the design block can be found. The design process of the different subsystems of the prototype is described. The critical parts due to the irregularity of the array are explained more in depth, particularly the antenna and the feeding lines. The final designs are shown and finally recommended improvements are presented and analyzed for future designs.

An extensive loss analysis of the feeding lines is presented in the fourth chapter. The cascade stages of the system are explained as well as the power limitations in the amplifiers due to their non-linear behavior. Both regular and irregular feeding networks are evaluated and compared under real design criteria to quantify the increase of losses due to the irregularity of the array.

In order to validate the work carried out in this project, the prototypes designed need to be tested first through simulations and later on through measurements. However, due to time constraints, only simulation results are included in this report. The validation is done in terms of the adaptive beamforming performance of the array and is presented in the fifth chapter. The final goal is to compare both regular and irregular arrays and demonstrate the improvement achieved with the latter.

Finally, some conclusions are drawn from the overall project and possible future lines are suggested in the final section.

## Chapter 2

# Optimum sparse array topology selection

A feasibility study is realized to select the optimum sparse array topology for the antenna panel operating at 26 GHz. However, before selecting the sparse layout, the antenna specifications should be clearly stated. After that, the criteria under which the topology should be chosen are explained. To evaluate the array under the loss criteria, novel design constraints are proposed for the placement of the ICs and the line length equalization with loss minimization as the goal. Later on, different sparse layout configurations are proposed and compared, adjusting them to the antenna requirements. Finally, the most suitable array topology for this case is selected to demonstrate the potential of aperiodic arrays for interference cancellation with high power efficiency.

### 2.1 Antenna specifications

As mentioned in the research approach, the sparse array should be able to reuse as much as possible from the demo antenna so the comparison is as fair as possible. Taking that into account and the input from NXP, the specifications of the antenna panel have been determined as follows:

- The array should cover the n258 frequency band (24.25 to 27.50 GHz).
- The array should have a sparse topology array consisting of 64 elements.
- The antenna elements of the array should be stacked circular patches used in the reference array given in Fig. 1.7.
- ABF (Analog Beamformer) ICs provided by NXP should be used to enable scanning.
- Antenna elements and the Beamformer Network (BFN) should be compatible with standard PCB technology.
- The array should be able to simultaneously operate with dual-polarization (H & V).
- The antenna elements should be spaced by at least  $\lambda/2$ .

- Line length difference between connector to IC and IC to the antenna should be kept to a minimum.
- Loss between ABF ICs and antenna elements should be as reduced as possible.
- Layout of RF splitter network should re-use as much as possible from antenna demo design.
- Interposer should be adapted to the existing panel so the heatsinks can be reused.
- The array should improve the EIRP ( $> 56$  dBm), reduce the sidelobe level to 20 dB for all visible space while keeping the scanning angle for a sector of  $\pm 45$  deg. in both elevation and azimuth.
- The array should have a beamwidth similar to the demo antenna (15 deg.).
- The thermal aspects of the array should be relaxed with topology and addressed with the heatsinks on board.

## 2.2 Criteria

The selection of which array topology would be optimum for this design is held under two criteria:

- On the one hand, the performance of the array should meet the specifications and requirements of the antenna panel, such as maximum sidelobe level, minimum EIRP, scan range, or beamwidth.
- On the other hand, the losses on the antenna feeding network should be minimized after the power amplifier, that is from the ABF IC to the antenna element. Then the cost function to be minimized is the loss on the lines feeding the patch antennas.

First, the algorithm from [1] is executed, which optimizes the topology in terms of maximum SLL by using the position-only control technique. This first step finds the optimal element locations that would match the expected performance of the array.

Once the element locations have been computed, the second algorithm computes an efficient clustering of the elements and finds out which is the maximum line length (or maximum loss) from IC to the antenna element. Each ABF IC can handle 4 RF input/output dual-polarized channels, so the antenna elements are clustered in groups of 4 elements using k-means clustering with equal size [25]. The routing is simulated as real as possible and can be seen in Figure 2.1, together with the routing of the demo antenna as a reference. It should be noticed that only one polarization is simulated, although an extra 1.2 mm is assumed in the IC pin to be able to route both lines of vertical and horizontal polarization preserving the minimum distance from the design rules and avoiding crosstalk between them. Finally, an extra 1 mm is taken due to the distance from the center to the feeding point of the circular patch.

$$L = 1.2mm + L_{routing} + 1mm \quad (2.1)$$

With those constraints on the routing, the algorithm determines the position of the chip, the pairing of elements and pins as well as the central location of the IC that minimizes the cost function of the losses. The outcome is later used in the design as a base for chip placement and feeding network

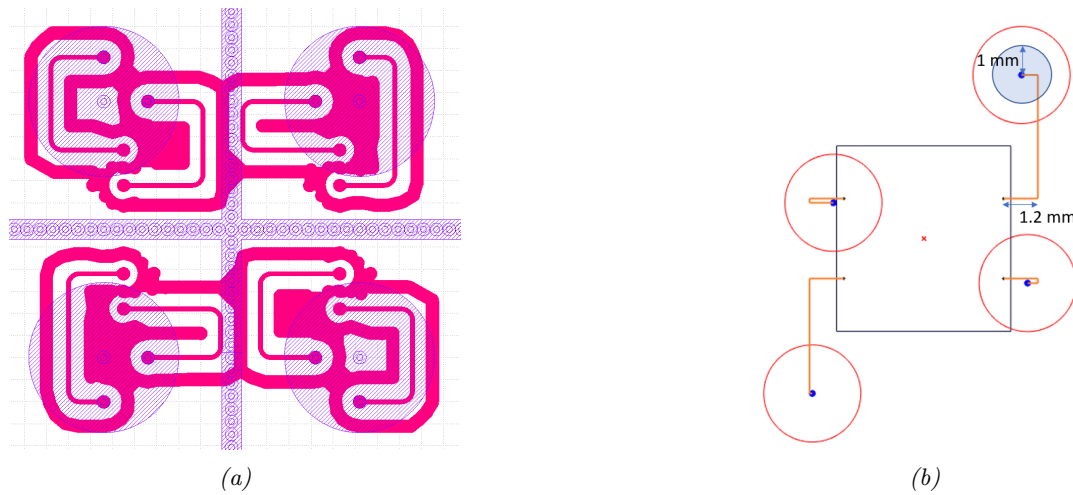


Figure 2.1: Routing from IC to antenna elements in (a) the design of reference array and (b) simulation of sparse topology

design. The clustering algorithm is executed 50 times and the one that minimizes the maximum line length is finally selected.

### 2.3 Analysis and comparison

The algorithm computes the optimum topology with the requirements set above and for different input specifications, such as the SLL minimization strategy and amplitude tapering profile of the array. There are two SLL optimization approaches available: minimization of the maximum side-lobe inside the field of view (FoV) or anywhere in the visible space (VS). The difference between both approaches can be seen in Figure 2.2, where the sidelobes of 2.2a are only reduced inside the sector window while in 2.2b are reduced everywhere.

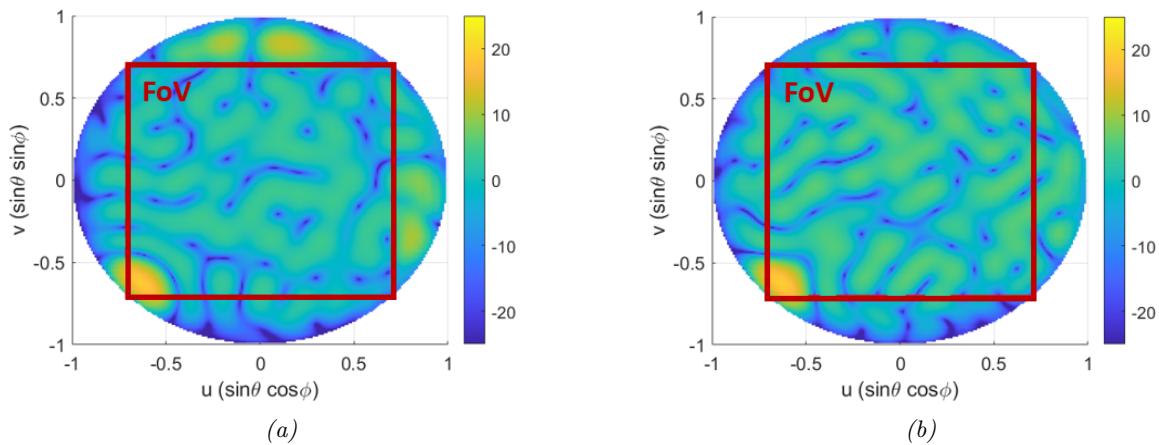


Figure 2.2: Radiation pattern of beam focused on the corner for SLL minimization within FoV (Array A) (a) and within VS (Array C) (b)

The embedded element pattern used as input for the layout optimization is a combination of the measured EEP of the regular array set as a reference. Namely, it is the average EEP of the elements in both polarizations that show a decent pattern. The final EEP assumed is shown in Fig. 5.3a.

Then, 5 fully aperiodic topologies are proposed with the field of view defined as the sector cell  $\pm 45 - by - \pm 45$ :

- Array A: Uniformly-fed, aperiodic, SLL minimized within the FoV
- Array B: Two Stepped-amplitude, aperiodic, SLL minimized within the FoV
- Array C: Uniformly-fed, aperiodic, SLL minimized within the visible space
- Array D: Two Stepped-amplitude, aperiodic, SLL minimized within the visible space
- Array E: Three Stepped-amplitude, aperiodic, SLL minimized within the visible space

As can be seen in Table 2.1, the uniform-fed arrays provide a good directivity, hence a high EIRP level that satisfies the requirement of  $> 56$  dBm. Although the maximum sidelobe level at broadside is below  $-20$  dB when the beam is pointing at the corner of the sector the interference level is too high. Both criteria are evaluated in the table since the EIRP value takes into account the estimated routing losses of each element, considering them all as the longest routing case of each topology. It is computed as in equation 2.2, assuming that the maximum available power per element is 20 dBm, corresponding to excitation amplitude 1.

$$EIRP(dBm) = Dir(dB) + P_{in}(dBm) - L_{max}(dB) \quad (2.2)$$

Table 2.1: Array comparison of proposed topologies for 45 deg.-by-45 deg. sector cell

| Array   | Broadside beam    |            |                   |                  | Corner beam       |            |                   |                  |
|---------|-------------------|------------|-------------------|------------------|-------------------|------------|-------------------|------------------|
|         | Directivity (dBi) | EIRP (dBm) | Max. SLL FoV (dB) | Max. SLL VS (dB) | Directivity (dBi) | EIRP (dBm) | Max. SLL FoV (dB) | Max. SLL VS (dB) |
| Array A | 23.7              | 60.3       | -22.2             | -22.2            | 20.3              | 56.9       | -15.1             | -6.7             |
| Array B | 23.3              | 58.1       | -25.5             | -25.5            | 21.9              | 56.9       | -19.0             | -12.7            |
| Array C | 23.5              | 60.0       | -20.5             | -20.5            | 20.5              | 58.6       | -13.3             | -13.3            |
| Array D | 23.0              | 58.0       | -23.8             | -23.8            | 21.8              | 56.8       | -17.5             | -17.5            |
| Array E | 23.1              | 57.0       | -25.1             | -25.1            | 22.2              | 56.0       | -18.8             | -18.8            |

Although the performance is improved with respect to the regular layout, the outcome parameters are not sufficient to meet the expectations due to the high maximum sidelobe level. As an alternative to reduce interference without losing EIRP, the number of elements should be increased or the sector definition should be changed. To keep a fair comparison with the reference antenna panel, the alternative chosen is to change the sector. Therefore, the new window used as sector cell for the base station antenna panel is now  $\pm 15 - by - \pm 60$ , taken as a good reference for covering both ground users and buildings in 5G cells [23]. Similar to the initial sector, the topologies analyzed are as follows:

- Array A: Uniformly-fed, aperiodic, SLL minimized within the FoV (Fig. 2.3a)
- Array B: Two Stepped-amplitude, aperiodic, SLL minimized within the FoV (Fig. 2.3b)

- Array C: Uniformly-fed, aperiodic, SLL minimized within the visible space (Fig. 2.4)
- Array D: Two Stepped-amplitude, aperiodic, SLL minimized within the visible space (Fig. 2.5)

Table 2.2 shows the performance results of the arrays with the new sector window and a clear improvement can be observed, particularly in the sidelobe reduction.

Table 2.2: Array comparison of proposed topologies for 15 deg.-by-60 deg. sector cell

| Array   | Broadside beam    |            |                   |                  | Corner beam       |            |                   |                  |
|---------|-------------------|------------|-------------------|------------------|-------------------|------------|-------------------|------------------|
|         | Directivity (dBi) | EIRP (dBm) | Max. SLL FoV (dB) | Max. SLL VS (dB) | Directivity (dBi) | EIRP (dBm) | Max. SLL FoV (dB) | Max. SLL VS (dB) |
| Array A | 23.5              | 60.0       | -27.4             | -14.7            | 22.5              | 58.9       | -24.9             | -12.2            |
| Array B | 23.6              | 60.3       | -32.2             | -18.2            | 22.2              | 57.2       | -29.8             | -12.0            |
| Array C | 23.6              | 60.4       | -22.5             | -22.5            | 22.6              | 59.4       | -20.2             | -20.2            |
| Array D | 23.4              | 58.3       | -25.6             | -25.6            | 22.8              | 57.7       | -23.4             | -23.4            |

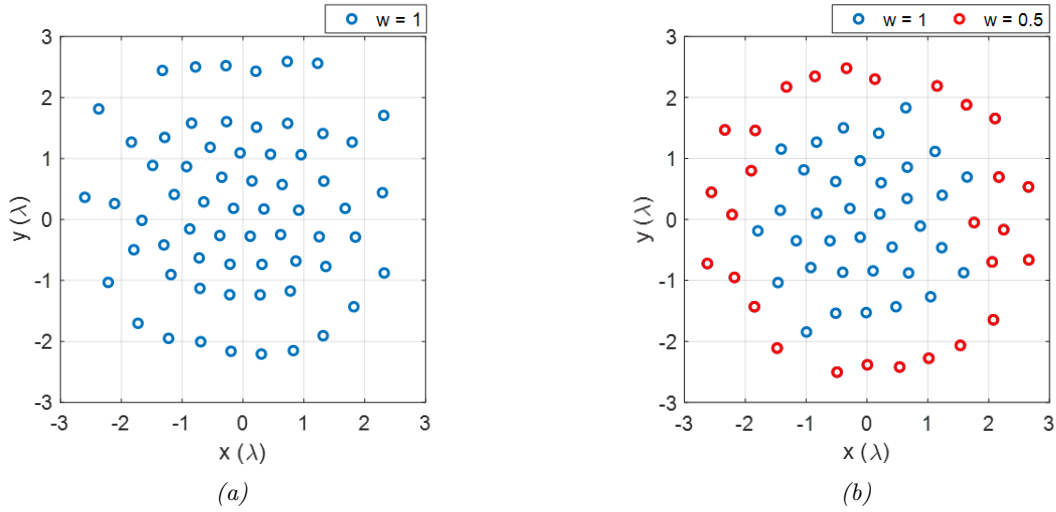


Figure 2.3: Topology of (a) arrays A and (b) array B

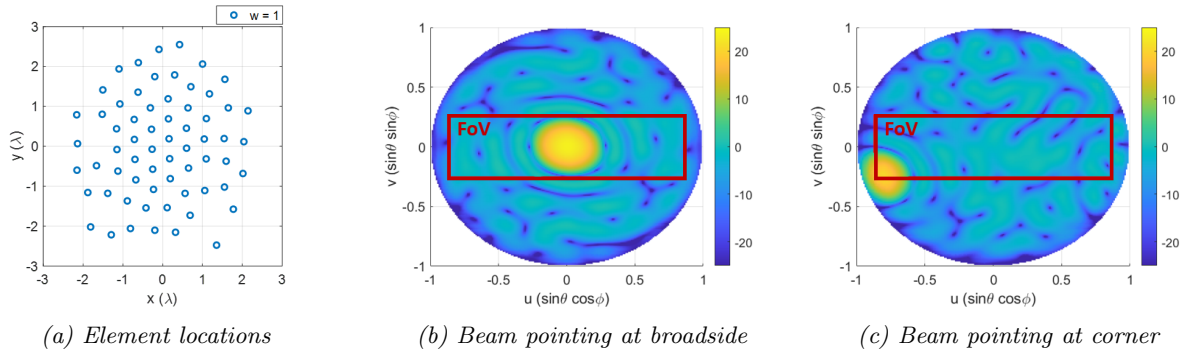


Figure 2.4: Topology and radiation pattern of array C

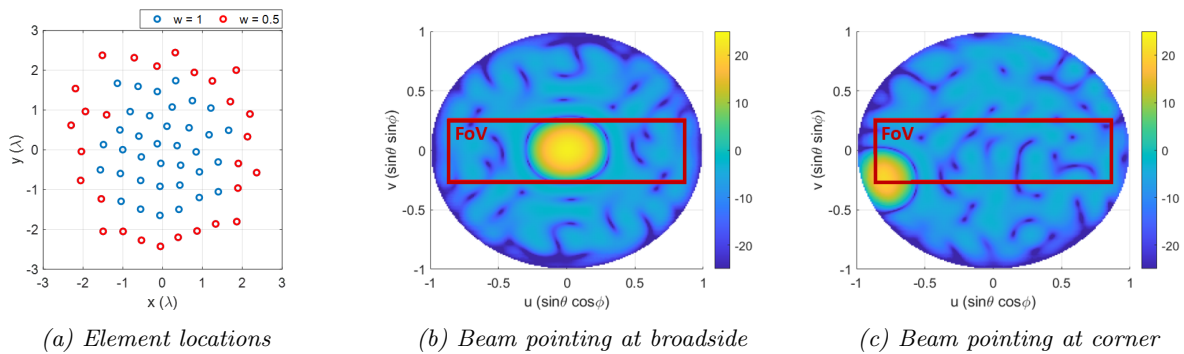


Figure 2.5: Topology and radiation pattern of array D

## 2.4 Conclusions

After analyzing and comparing the estimated performance of each array topology, the one to be used in the design should be selected out of the arrays using the 60-by-15 sector cell from Table 2.2. Regarding first the optimization approach, the arrays where the SLL has been minimized within the field of view suppose very high sidelobes outside the sector window. Although it can be very useful for space applications, 5G base stations would create a lot of interference between users, especially when the beam is pointing at the corner of the cell. Therefore, arrays A and B are discarded due to the maximum sidelobe of -12 dB that can interfere with other users.

Then, the best options for this application are the arrays C and D since they present lower sidelobes in the whole visible space, at the cost of an increase of the SLL within the sector. Array C provides higher EIRP and the SLL is good but near the -20 dB limit for the corner beam. The stepped-amplitude feeding is a good approach to improve the sidelobe level yet the EIRP is reduced.

To maximize the coverage of the base station, the uniformly-fed array C is preferred for the realization of the antenna panel. In case the actual SLL results to be lower due to the approximations done (the same EEP assumed for all the elements and both polarizations taken from the regular structure), the SLL can be potentially improved through the control chip. Therefore, lower sidelobes can be achieved with amplitude-phase control. However, not as effective as the layout optimized with the particular amplitude-phase distribution. Based on these arguments, array C is the one selected to move forward with the design of the antenna panel.

If the selected array (array C of Table 2.2) is compared with the presented state-of-the-art regular arrays from Table 1.1, a huge improvement can be easily noticed. The SLL reduction is improved by 9.5-12.5 dB with respect to the regular arrays from the previous section. In conclusion, the enhancement of sparse array topology is clear in terms of interference suppression.

## Chapter 3

# Design of aperiodic phased array

Once the most suitable topology to realize for this case is determined, it is time to start designing the antenna array. Advanced Design System (ADS) from Keysight is used to carry out the design and execute the simulations. The design of the regular antenna panel is used as a baseline for this design. In this chapter the design of the antenna panel and its subsystems are explained together with some validations through simulations. The complete design validation is available in the following chapters.

### 3.1 Board technology

The stack-up of the board is composed by 12 layers as shown in Figure 3.1. Astra MT77 is the dielectric used for the PCB with a dielectric constant  $\epsilon_r = 2.95$  for the prepreg and  $\epsilon_r = 3$  for the core substrate. The upper layers are used for the antenna part and are separated by layer 6, which contains the ground plane for the antenna array and decouples its design with the other subsystems. Below that, the bottom layers contain the routing of the feeding network, control signals and chips on the bottom.

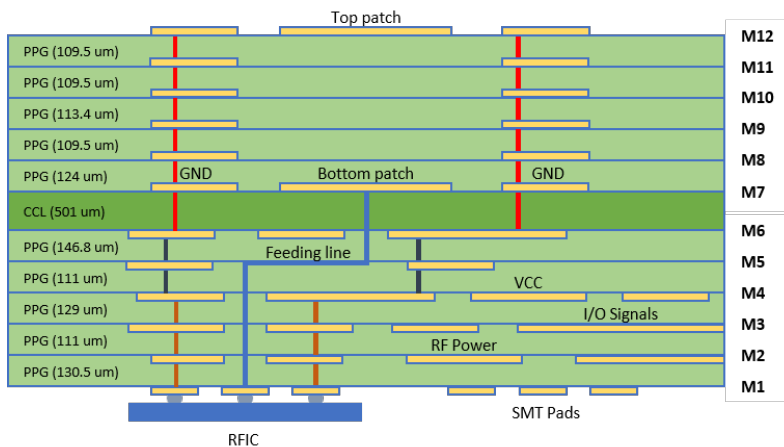


Figure 3.1: 12-layer substrate Astra MT77

## 3.2 Antenna block

Although the antenna element is similar to the one from reference panel, its structure has been modified to suit the new topology. In this section, the design, tuning and simulation results of a single antenna element are presented. Once the single element is optimized for the new layout structure, the antenna array is designed with the selected layout topology.

### 3.2.1 Single element

In the reference antenna array, the antenna element is a circular pin-fed stacked-up patch with a squared fence for element isolation. However, the irregularity of the layout requires another fence shape in order to not overlap with the clearance area of other antenna elements. Therefore, a circular fence is used so that only the vias on the fence are overlapped in some cases, but it is not critical while the inner area is kept clear. The 3D model of a single antenna element is shown in the figures below.

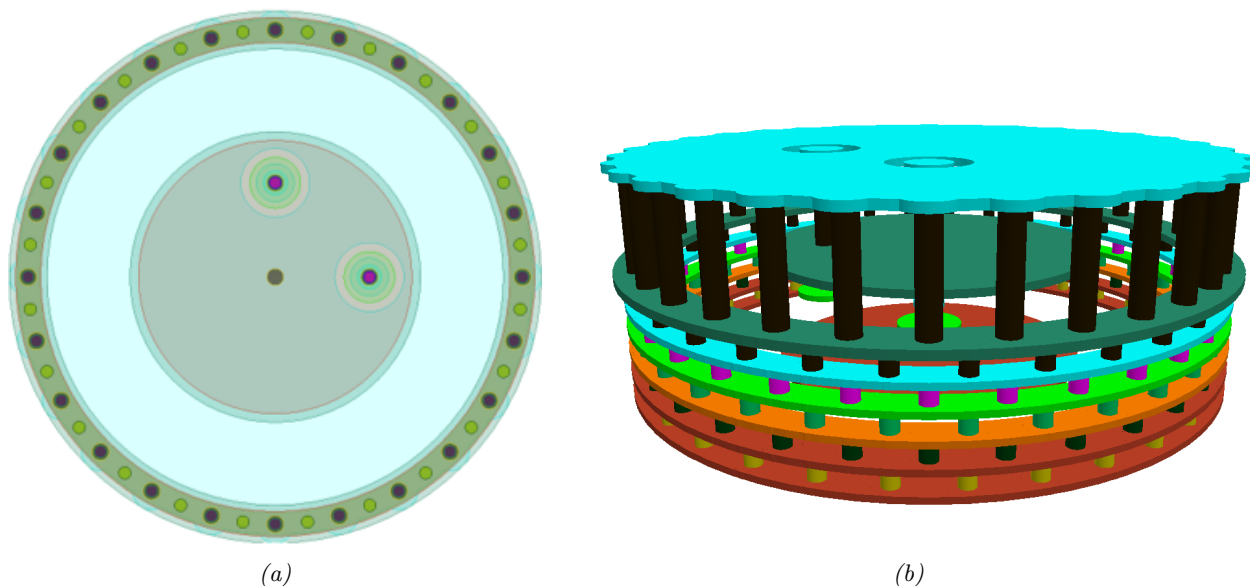


Figure 3.2: Antenna unit cell in from (a) top view and (b) side view

The modification on the fence has slightly affected the reflection coefficient of the single antenna. In order to tune the antenna with the new geometry, the feeding points are moved to 1.1 mm with respect to the center of the patch. The resulting S-parameters are shown in Figure 3.3. The bandwidth of the antenna is extended from 24.75 GHz to 27.25 GHz, which is a bit compromised but quite good for the desired band.

The radiation pattern of the single antenna is also checked to validate the modified antenna layout. The field cuts at 26 GHz can be seen in Figure 3.4 which accurately corresponds to the expected radiation pattern of a patch antenna.

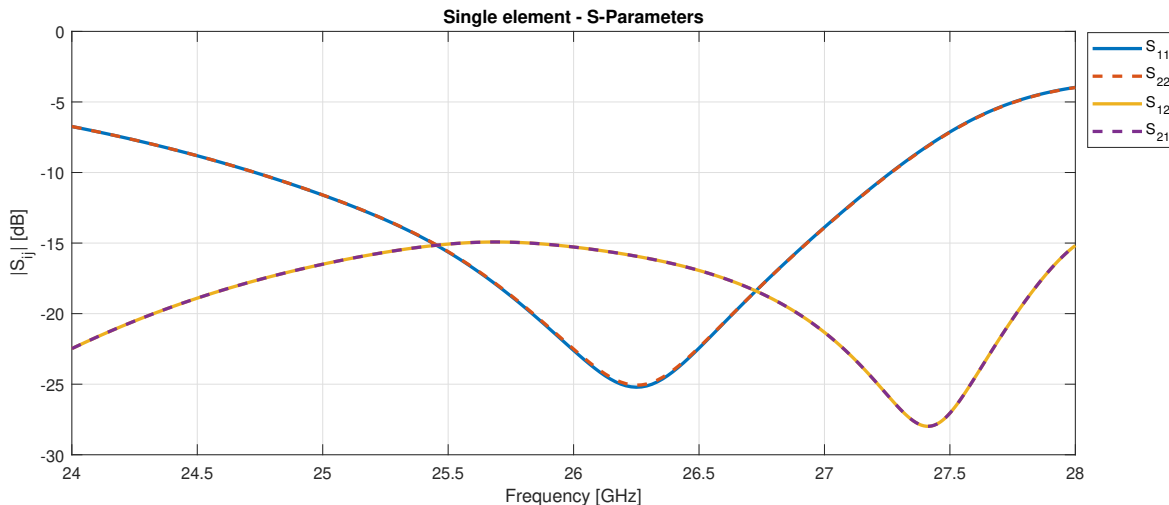


Figure 3.3: Simulated S-Parameters of an isolated antenna element

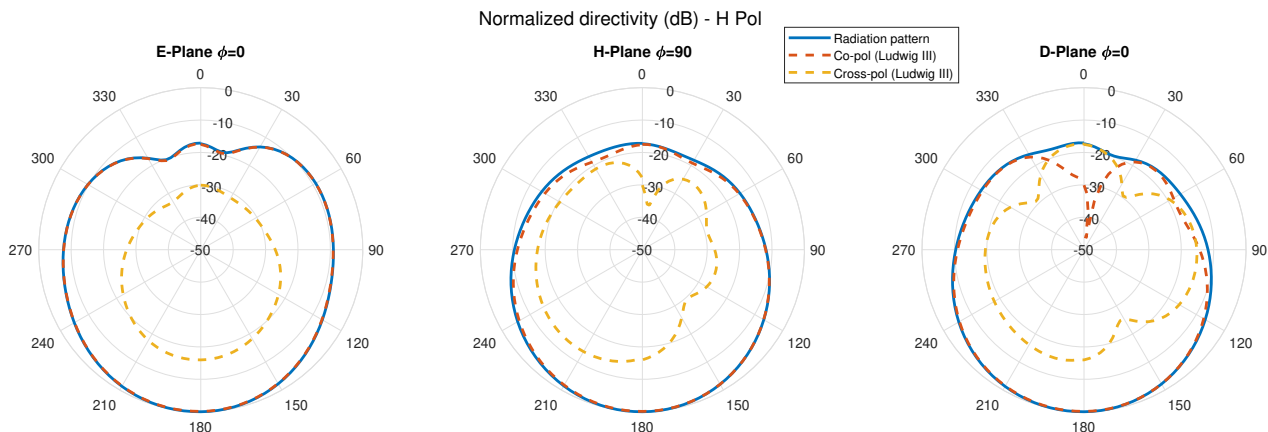


Figure 3.4: Far field cuts of single antenna element

### 3.2.2 Antenna array

After several iterations of beamforming analysis through full-wave simulations, the final antenna array looks like in Figure 3.5. At the initial simulations, the interference cancellation was not satisfactory caused by the significant difference among the embedded patterns of the antenna elements due to the mutual coupling, resulting in an averaged EEP not representative for all the elements.

In order to overcome the differences in the pattern among the elements, the mutual coupling has been reduced by improving the isolation of the antenna element. The fencing of the antenna is now more dense with more number of vias and consequently, less spacing between them. Ground planes are placed in all layers where no elements are located to avoid diffraction on the radiation layer and ground vias are also placed where the antennas are not closely spaced for a better isolation. After a couple of iterations, the final results of the simulated array are satisfactory and presented in Section 5.

It should be noticed that the irregular sparse array is larger than the regular one with the elements spaced by half-wavelength. The aperture size in the regular array is 40.39 by 40.39 mm, while the irregular one is now 49.39 by 57.97 mm. Taking the largest dimension, the antenna aperture has been increased by 43.5% due to the sparsity of the array.

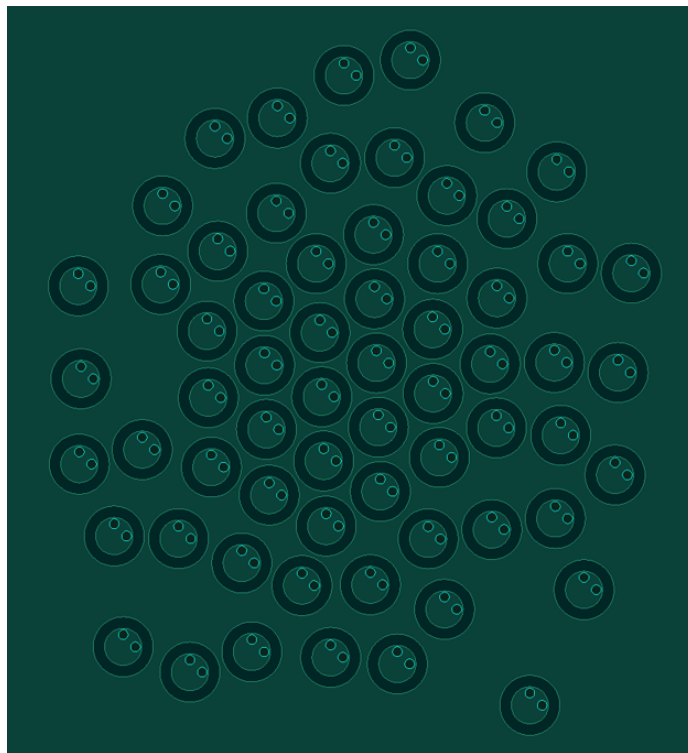


Figure 3.5: Design layout of the aperiodic array with circular patch antenna elements

### 3.3 Feeding network

The transmission lines of the feeding network are designed as in the reference array. A stripline on layer M5 connects the IC RF pins with the corresponding H or V feeding point of each patch (Fig. 3.1). However, the irregularity and asymmetry of the array implies a non-straight forward routing. It is important to simplify or avoid calibration on the front-end of the antenna array [15]. In order to do so, the feeding lines are aimed to have the same electrical length in all the channels. Then, the losses and phase shift in each element are the same after the beamformer chip.

From the algorithm that simulates and optimizes the routing of the feeding lines, the output of the chip placements is used as an initial point of the design and from there, manual iterations are done to find the optimal placement with equalized feeding lines with the minimum loss. The feeding network is displayed in Figure 3.6a, where clusters of 4 elements are formed in each IC location.

The stripline on M5 is surrounded by a ground on the same layer with vias going to the upper and lower layers (M6 and M4) in order to avoid cross-talk with other near striplines. Also, a ground on M6 is covering all the stripline area so that isolation and a good ground plane is ensured. The resulting network in a single cluster is shown in Figure 3.6b.

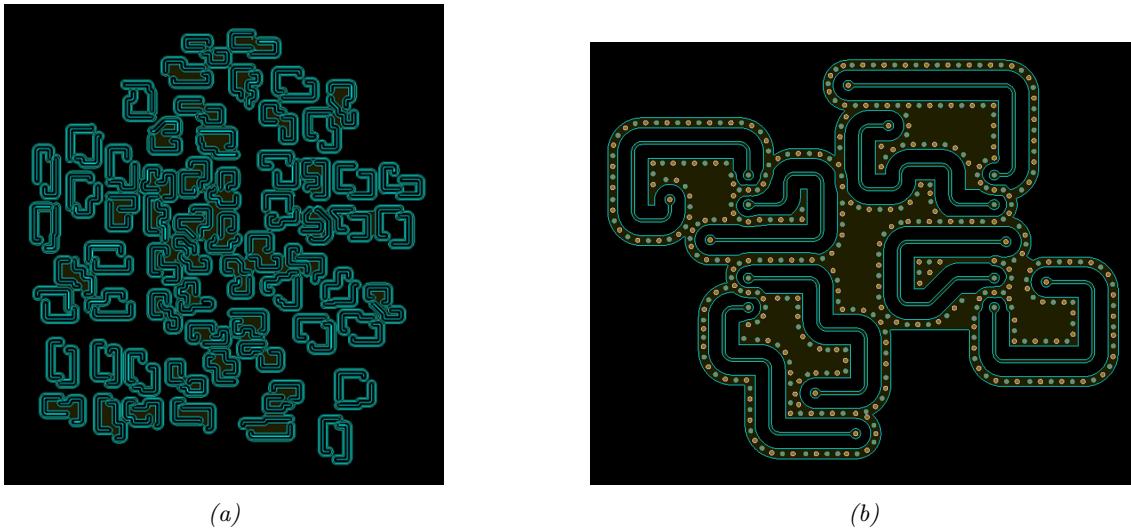


Figure 3.6: Feeding (a) network and (b) lines of a single chip 4 dual-polarized element cluster from irregular array design

### 3.4 Distribution network

For the RF signal distribution from external connectors to the beamforming ICs, Wilkinson power dividers are used to split the RF signal with high isolation among the ports. Microstrip lines are used on the top layer mainly for vertical polarization and striplines on layer M2 for most of the horizontal polarization lines. Both transmission line structures are used to allow crossing the signals when needed and to provide a better isolation between the signals.

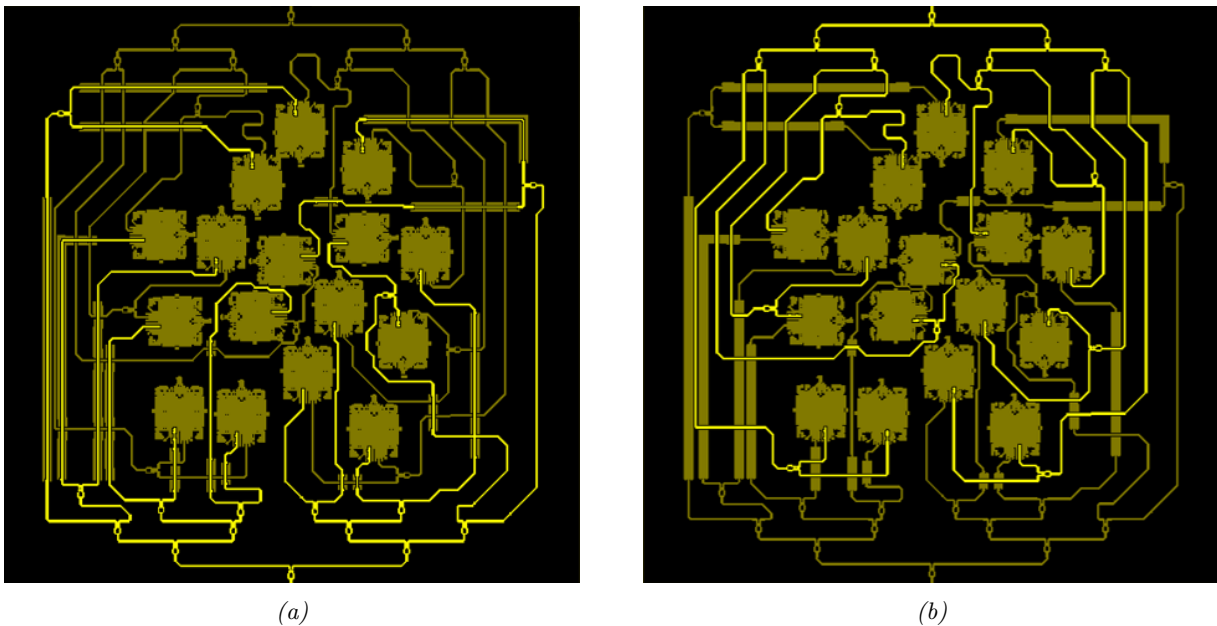


Figure 3.7: RF distribution network on for (a) horizontal and (b) vertical polarization

A calibration of the chips will be needed since the lines for each chip have different lengths. However, the dynamic range of the amplitude calibration has been reduced by using the same amount of Wilkinson splitters for each signal path and in some cases where the lines are very short, a meander line has been used to make it slightly longer. The distribution network can be seen in Figure 3.7, where the signal for vertical polarization comes from the connector on the top and the horizontal one from the bottom of the figure.

For a proper calibration and loss analysis completion, a test board is designed in order to validate the simulations results through measurements. Its final design is shown in Figure 3.8.

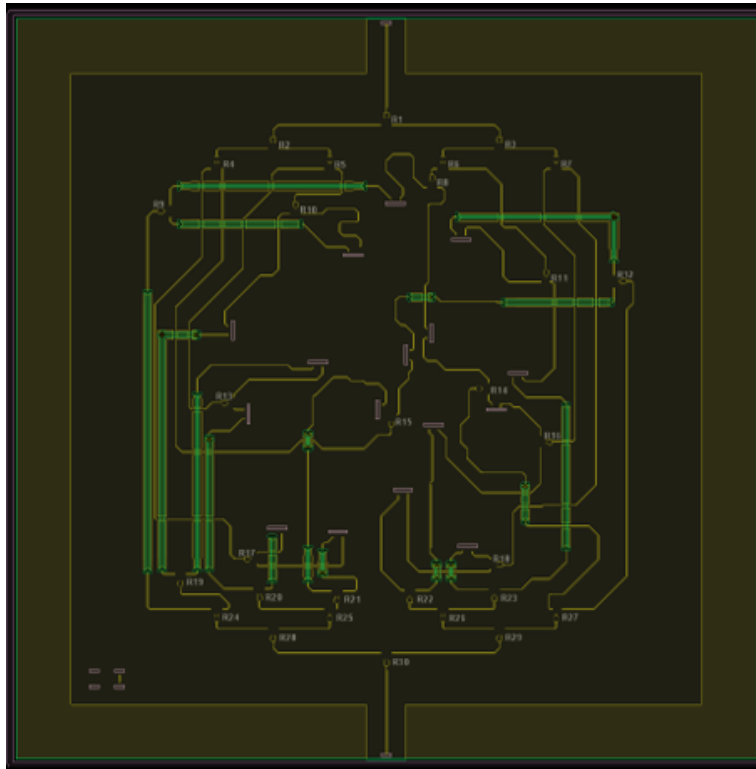


Figure 3.8: Layout of the test board from top view

### 3.5 Control signals

The adaptive beamforming is configured with the beamformer IC settings, which are controlled via SPI (Serial Peripheral Interface) interface through LVDS (Low-Voltage Differential Signaling) signals for a high communication speed. The ICs are divided in two groups of eight chips controlled by an FPGA (Field-Programmable Gate Array). In Figure 3.9a the pins location are shown on the chip. On the top of the chip, the clock and data input and output signals are connected from chip to chip. On the bottom, the chip select and the TDD[1:0] signals to determine the RF function of each channel.

The routing of the control lines is on layer M3 and some on layer M2 when needed, as can be seen in Figure 3.9. The FPGA is connected on the right of the panel so all lines are routed to the right.

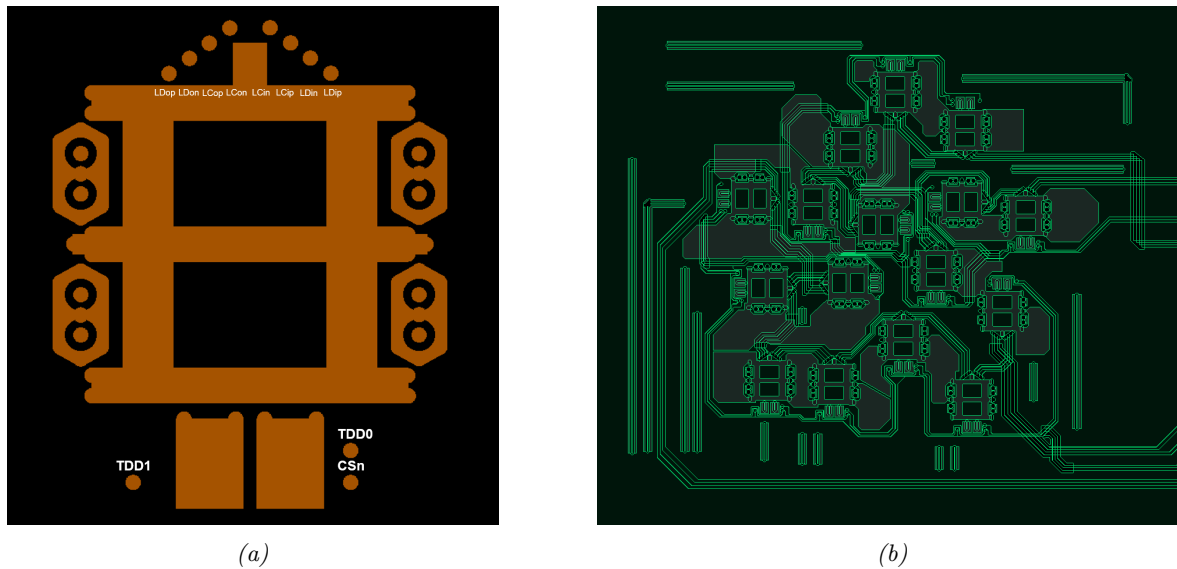


Figure 3.9: Control signals (a) pins on the beamformer chip and (b) their routing in the panel

### 3.6 Supply network

The supply of the beamforming chips is mostly on layer 4 and connected to the chips through the copper areas on the above layer. The copper layers are placed as wide as possible in order to avoid capacitance effects due to narrow lines. Moreover, the supply network has been divided into 8 sections to reduce the noise. Each of the sections is feeding 2 ICs from one DC connector of the panel, as shown in Figure 3.11.

For the proper operation of the beamforming ICs, it is important to ensure that the supplied voltage is within the upper and lower limits set on the ICs specifications. A maximum of 20 mV voltage drop is set as a requirement to ensure this. Therefore, a DC simulation is performed in order to determine the voltage drop on the supply lines. The simulation is executed with MoM (Method of Moments) ADS simulation engine at a very low frequency and low-impedance sources placed at the locations of the DC connectors.

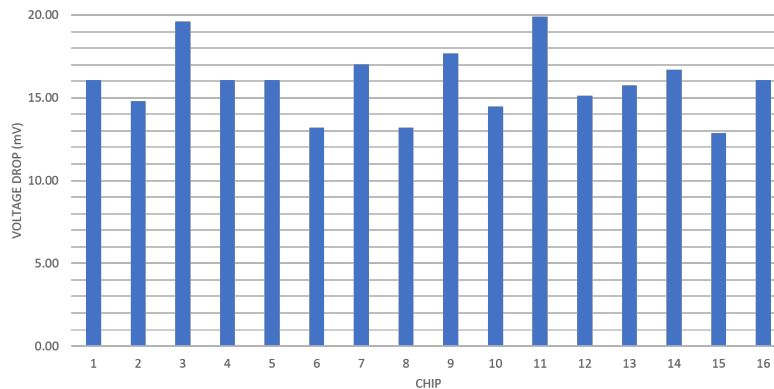


Figure 3.10: Voltage drop levels of each chip from DC connectors

For each of the chips, the voltage drop has been computed from the transmission coefficient  $S(i, j)$ , being  $i$  the chip number and  $j$  the connector from the corresponding network. The numeration of the elements is represented in Figure 3.11. The voltage source at the connector is assumed to be the nominal one required by the chips (2.8V).

After a few iterations of design modifications to minimize the voltage drop and satisfy this requirement, the results can be found in Figure 3.10. All the cases are within the voltage drop limit specified. Therefore, the drop on the voltage lines has been successfully validated and all the beamforming chips can be fed with a minimum voltage of 2.78V.

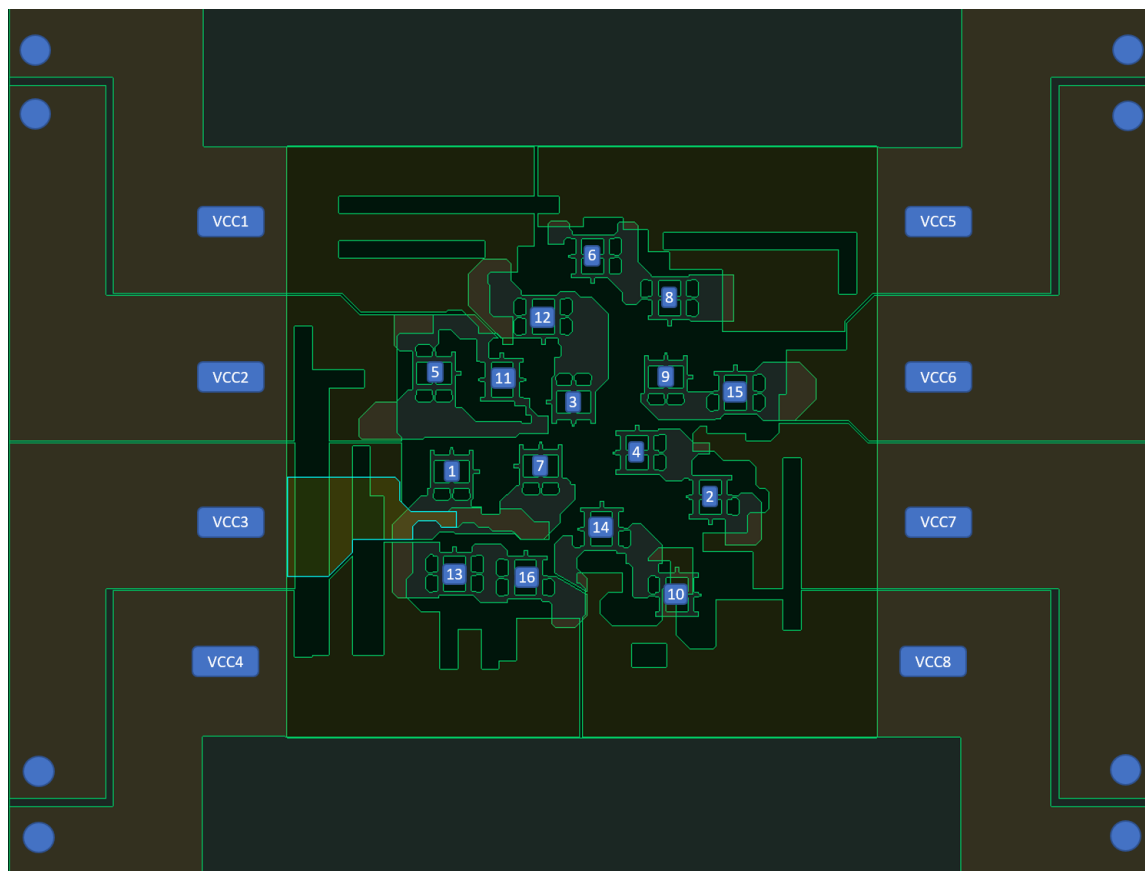


Figure 3.11: Supply network of the irregular array panel

### 3.7 Panel design

Finally, once the design of the aperiodic antenna array system is finalized, the panel is ready for validation and to be manufactured. The top view can be seen in Figure 3.12 and in Appendix A in more detail. On the laterals of the panel, the RF connectors are located for each signal polarization. The DC connectors for the supply network are banana connectors on the corners of the panel, close to the decoupling capacitors. Also, microFarad decoupling capacitors have been placed around the array area and nanoFarad capacitors near the chips.

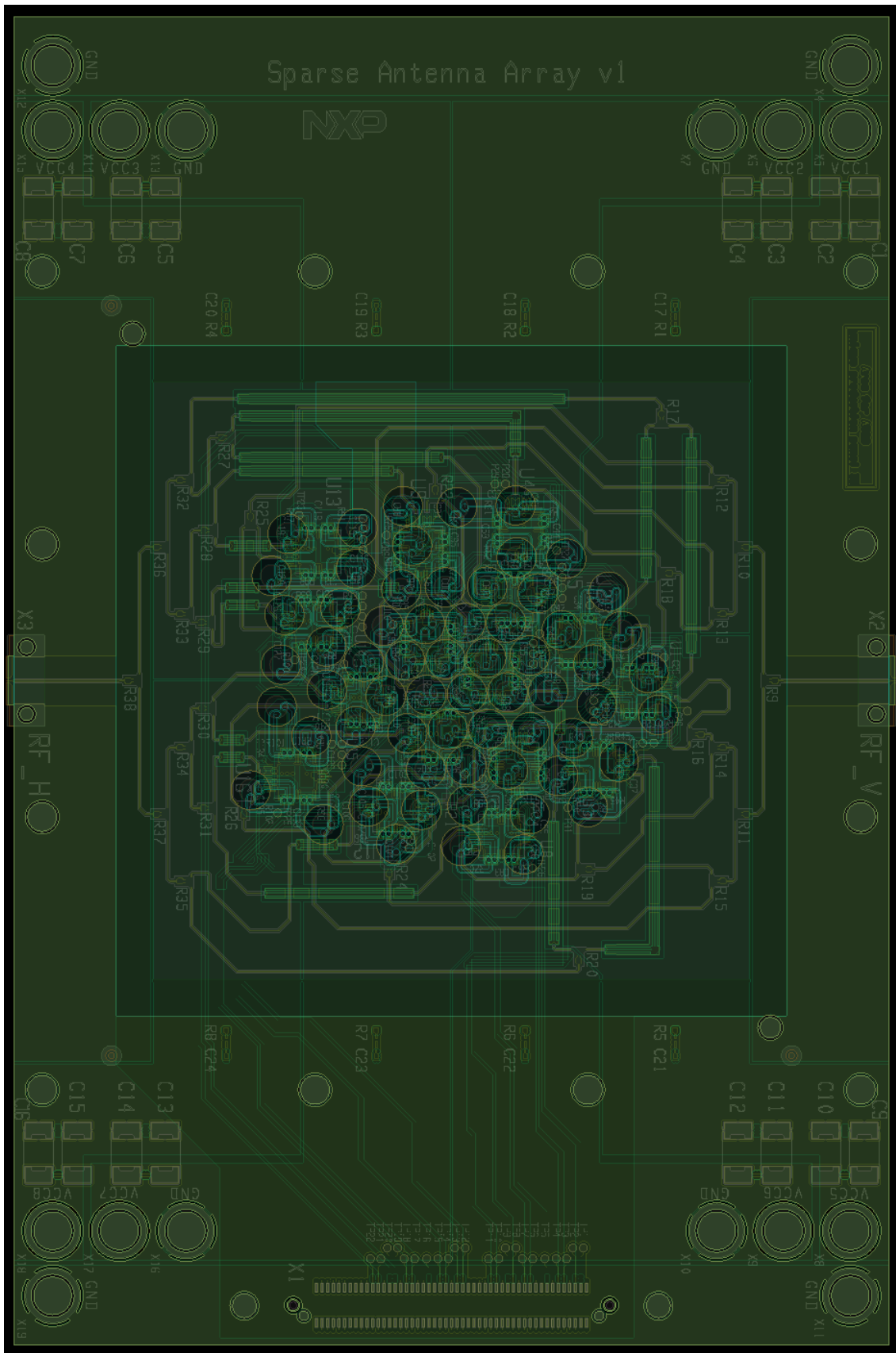


Figure 3.12: Panel layout top view

### 3.8 Recommended improvements

In this section some approaches are proposed as future lines in order to improve the antenna array in a future design. Due to the limited time span of the thesis, these features are not implemented in the current panel design but yet detailed and some features validated through simulations.

#### 3.8.1 Dual-polarization array layout optimization

For the synthesis of large irregular sparse array, usually idealized antenna elements are assumed. This usually leads to a suboptimal configuration of the antenna array topology because the mutual coupling among the elements should be taken into account [26]. In this case, the embedded element pattern is measured in a similar antenna element placed in a regular grid. Although it does take into account the mutual coupling, the assumption of the average EEP as a good approximation is not completely valid since there are two different polarizations being used, each of them leading to a different radiation pattern on the antenna element. As seen in Figure 5.4, the embedded element pattern changes substantially depending on the direction of excitation. This discrepancy makes the used topology a suboptimal topology that does not achieve the targeted performance and reduced interference.

The iterative algorithm optimization used from the position-only control technique [14] follows the two step optimization scheme shown in Figure 3.13a. This technique already accounts for the presence of strong mutual coupling and includes it efficiently on the second step.

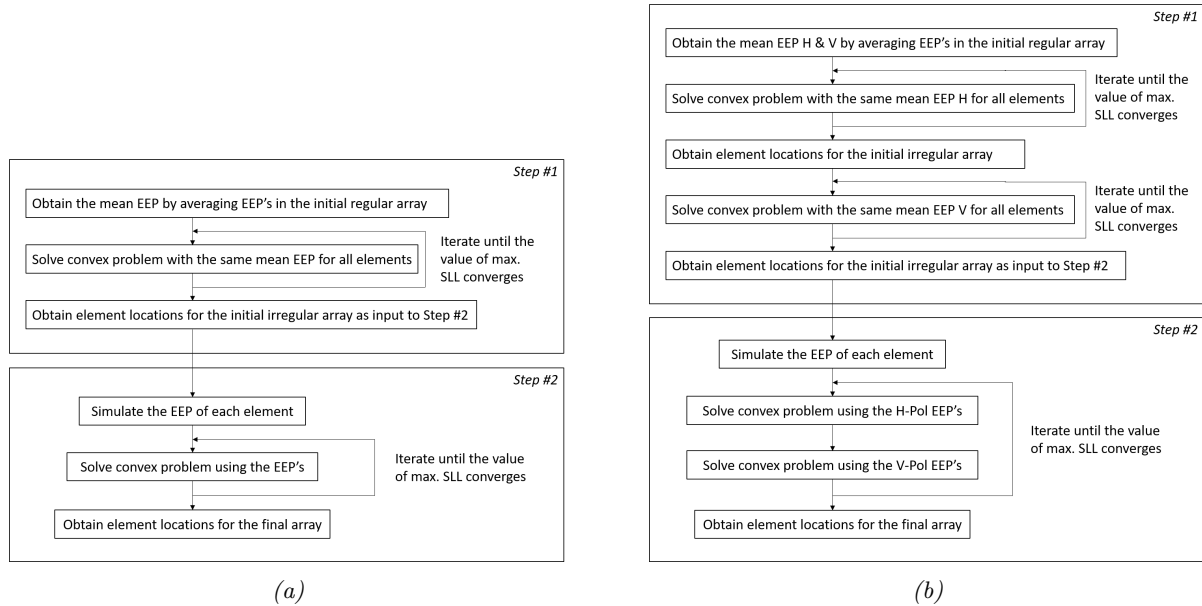


Figure 3.13: Optimization scheme for (a) single polarization and (b) dual polarization

In case of a dual-polarized antenna array, the scheme should be slightly modified in order to obtain an optimal configuration for both polarization cases. Figure 3.13b presents the proposed modified scheme that could improve the performance of the dual-pol array by iterating with the EEP from one polarization and then with the EEP from the second polarization, repeatedly until a good maximum SLL value is achieved.

Although the proposed algorithm has not been tested due to limited time, it is believed that the proposed modification would improved the final beamforming performance thanks to the co-optimization of both polarizations.

### 3.8.2 Sequential rotation of the antenna elements

Microstrip planar antennas have many benefits such as easy fabrication, compact structure and low cost. However, these are typically narrowband antenna elements. Mirroring the feeding points and applying a phase shift on the elements offers a low VSWR (Voltage Standing Wave Ratio) over a wide frequency band. [27]. Sequential rotation of the elements is a widely used technique to symmetrize the radiation pattern and improve the axial ratio, thus reducing cross-polarized signal and increasing the antenna array performance [28] [29].

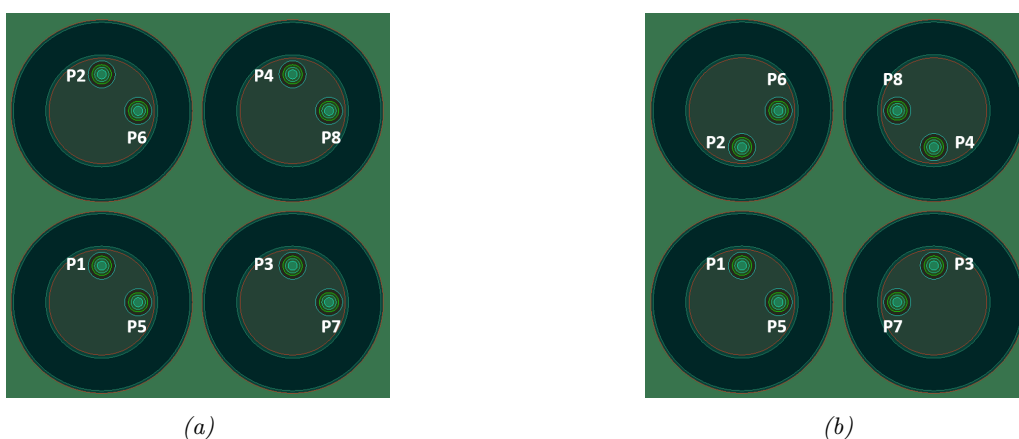


Figure 3.14: Cluster of regular antenna (a) without and (b) with sequential rotation

The disadvantage of sequentially rotate the antenna elements is the increase of complexity on the feeding lines design. Since this is something already addressed in the current design due to the irregularity of the array layout, it would not be an actual increase of complexity in this case.

An example of the mirroring of the feeding points can be seen in Figure 3.14 for a single cluster of a regular array. While in the regular structure is quite straightforward how to mirror them, in the irregular layout is not that simple.

As a first step the 2x2 arrays from Figure 3.14 are analyzed through full-wave simulations. The improvement is clearly seen on the reflection coefficient in Figure 3.15, where the resonance obtained with sequential rotation is better within the bandwidth of interest. The most noticeable improvement is on the ports that are facing the external part of the array (Ports 2, 4, 7 and 8): their reflection coefficient in Figure 3.15a shows a narrower resonance. By contrast, with the sequential rotation all pins are in the inner part of the array and the S-parameters are much similar among the ports, so the edge array effect is solved.

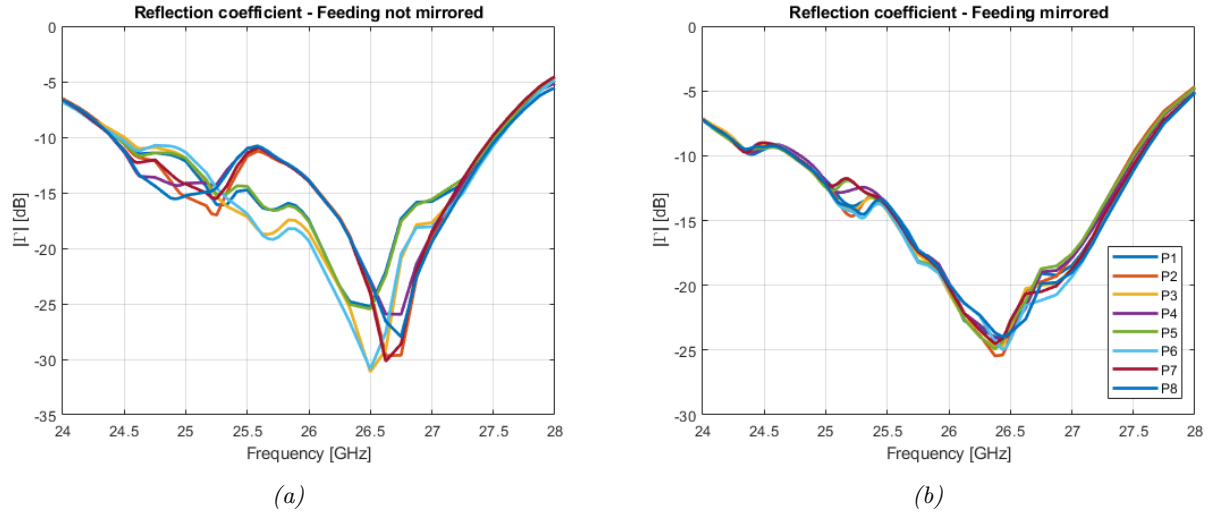


Figure 3.15: Reflection coefficient of regular antenna cluster (a) without and (b) with sequential rotation

As a consequence, the VSWR curve is also improved as it is shown in Figure 3.16. As seen in the reflection coefficient, all the channels have a similar VSWR over the observed frequency band in the mirrored case. Therefore, the overall VSWR has been reduced and the element location in the array is not relevant for its performance as it is without sequential rotation of the feeding points. In other words, the antenna elements are better matched to the transmission lines so more power is delivered to the antenna and the embedded element pattern can be more uniform over the different elements.

$$VSWR = \frac{1 + |\Gamma|}{1 - |\Gamma|} \quad (3.1)$$

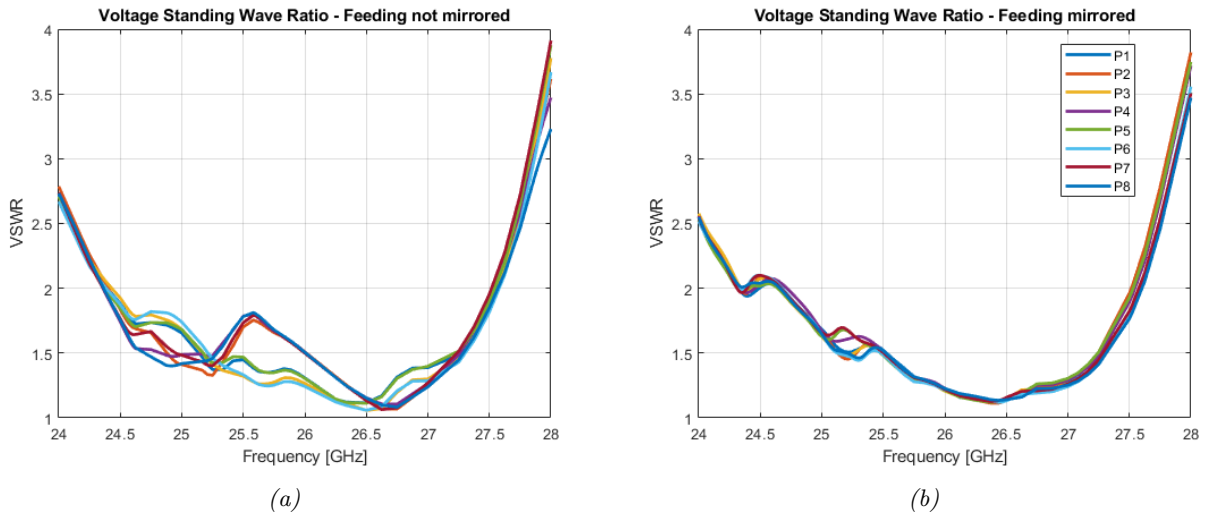


Figure 3.16: VSWR of regular antenna cluster (a) without and (b) with sequential rotation

In Figure 3.17, the current irregular array without any rotation is shown together with a proposed sequential rotation on its feeding points. The reflection coefficient at the central frequency is evaluated and compared between them in Figure 3.18 for all the channels of the array. Overall, the resonance is strongly improved with the feed mirroring. The average reflection coefficient of all channels at the center frequency is improved by 2.63 dB due to the feed mirroring of the elements.

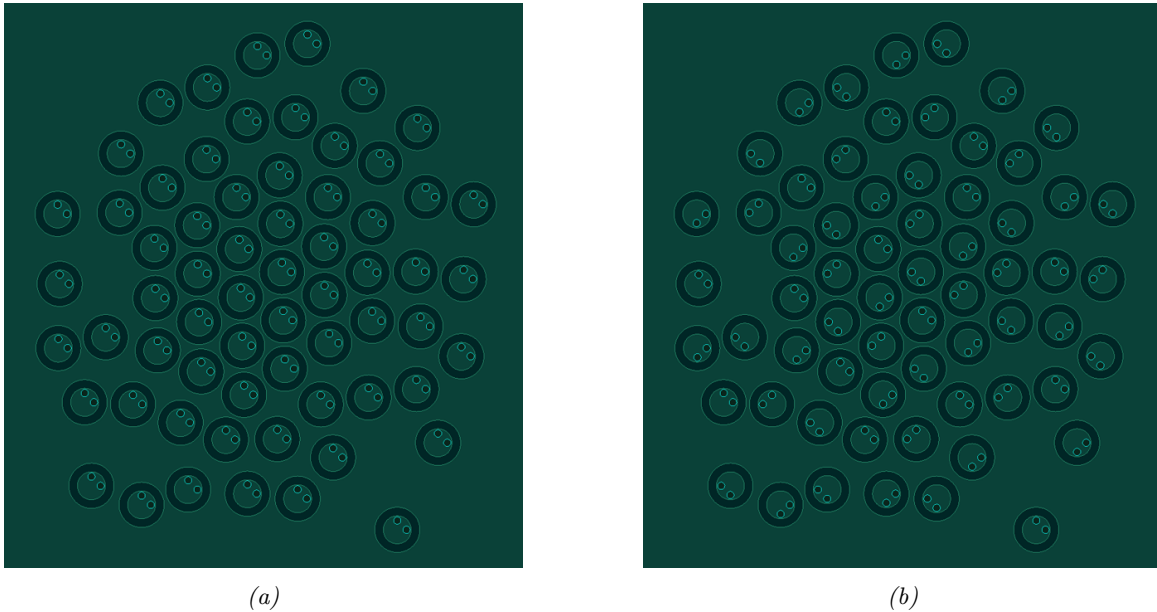


Figure 3.17: Irregular antenna layout (a) without and (b) with sequential rotation

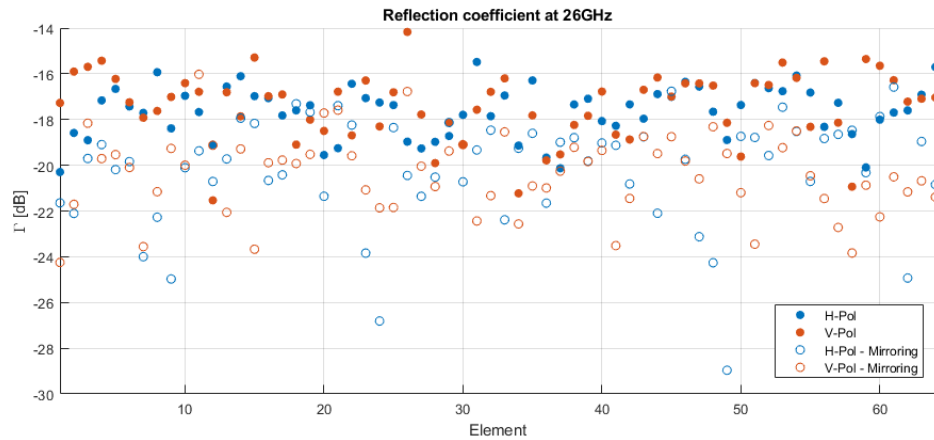


Figure 3.18: Reflection coefficient comparison with regular and mirrored feeding

The antenna performance is similar to the non-mirrored feeding from the radiation point of view, no significant improvement is seen in the EEP symmetry. Although there is still a strong polarization influence on the patterns, mirroring the feeding is a good alternative to improve VSWR and probably also the operational bandwidth. Due to limited computational resources, the performance has only been simulated at the central frequency instead of over the band.

### 3.9 Conclusions

Through this chapter the design process has been explained in detail and the final layouts of the panel board and test board are meant to be manufactured. Before that, the validation through simulations has been done to ensure that the targeted performance is achieved before the prototype is realized, shown in the following chapters. Due to the issues detected during the validation, some solutions are proposed in this chapter to overcome them in the future and achieve a better design.

The main work has been on the antenna array and its iterations on the design for reducing the coupling effect among the elements. Another critical part of the design process has been the feeding network, where the line of each channel has been equalized but reducing as much as possible the length in order to minimize losses in the front-end. The other blocks of the antenna system have also supposed a challenge due to the irregularity of the whole layout. Finally, the design of the irregular feeding network with multi-channel mm-wave beamforming chips is accomplished.

## Chapter 4

# Analysis of losses

In this chapter, an extensive analysis of the losses is conducted to evaluate the impact of the array irregularity on the losses in a complete design. In addition, the loss analysis is used for planning a proper calibration using the phase shifters and amplifiers in each beamforming IC.

There are two feeding networks used in the panel antenna: the first one corresponds to the feeding lines from the beamforming ICs to the antenna feeding points (after the power amplifier), named feed network. The second network is referred to as the distribution/splitter network and corresponds to the lines from the RF connector of the panel to the beamforming ICs (before the power amplifier). A diagram of the different stages of the cascade system is shown in Figure 4.1.

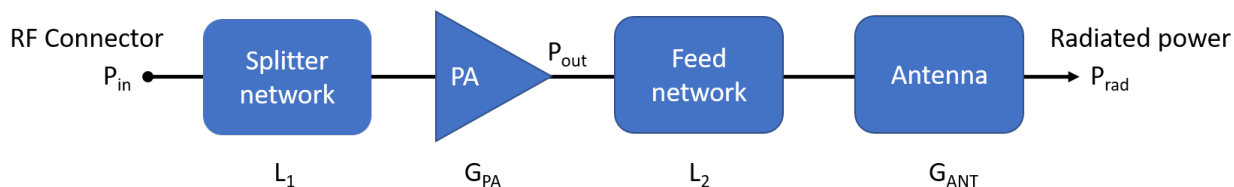


Figure 4.1: Stages of the cascade system from board connector to radiation in transmission mode

While the losses on the feed network directly affect the radiated power of the array and its power efficiency, the losses on the splitter network can be recovered by the variable gain of the amplifier. However, the output power of the PA is limited due to its linearity, so increasing the amplifier gain cannot compensate for the losses on the front-end because  $P_{out}$  has to be below its saturation point. From the receiving point of view, the losses on the distribution network are masked by the LNA.

The output power of the amplifiers is limited by its compression point at 1 dB, at which the output power is compressed by 1 dB due to non-linear behavior (Fig. 4.2a). Furthermore, the commonly used Orthogonal Frequency Division Multiplexing (OFDM) in wireless communication sets a high Peak to Average Power Ratio (PAPR) that limits, even more, the average output power level on the amplifier. The motivation is to guarantee that the peaks of the OFDM signal are inside the linear region of the PA, such that the non-linear behavior does not lead to signal degradation in form of harmonic distortion and adjacent channel interference (Fig. 4.2b) among others [32] [33].

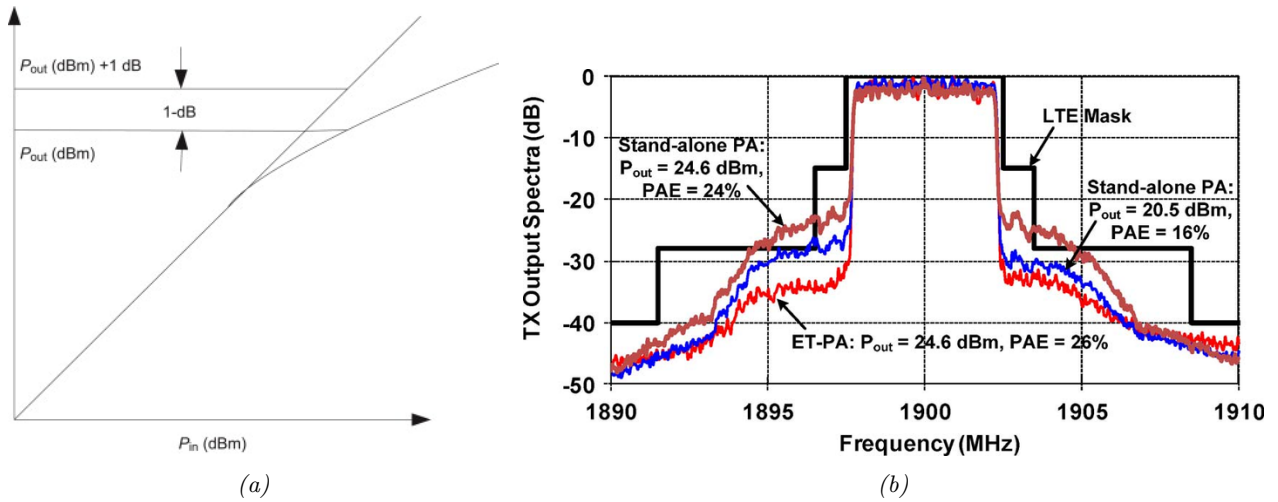


Figure 4.2: Non-linear behaviour of power amplifiers: (a) 1-dB compression point as a function of input versus output power [30] and (b) adjacent channel leakage on LTE band [31]

Due to these limitations, the amplifier in the regular array works at the back-off region so there is still a margin to increase the gain for the splitter losses compensation. This means that there is a margin of several decibels by which the losses can increase without degrading the power efficiency of the antenna array system.

#### 4.1 Feeding network

Since the transmission lines on the feeding network are located after the power amplifier, their calibration is very critical and it is preferred to ensure that they are calibrated by design. Therefore, all lines have the same length so each channel goes through the same line loss and phase shift. The feeding lines for a single cluster with 4 dual-pol. channels is shown in Figure 4.3.

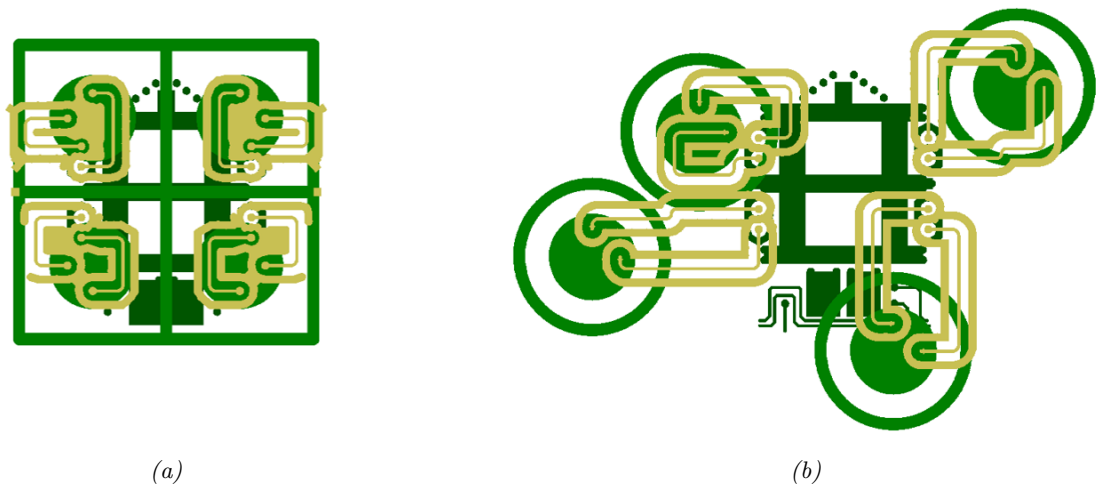


Figure 4.3: Feeding network of one 4-element dual-pol cluster in (a) regular array and (b) irregular array

The results of the characteristics of each feeding line plotted in Figure 4.4 show small variances among them: the maximum difference on phase shift is 7.58 deg. and the power loss coefficient varies 0.15 dB. If the beamforming performance is evaluated with the loss and phase variation on antenna feeding points, the influence on steering beam direction is negligible. The impact on the sidelobe level reduction is positive since it is enhanced around 1dB in most of the cases thanks to the amplitude tapering profile created by the small variances on amplitude.

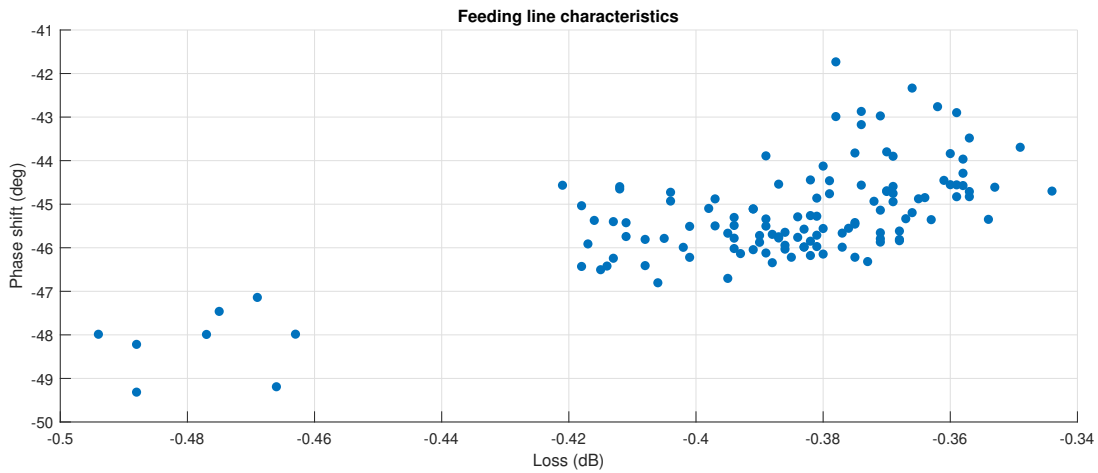


Figure 4.4: Distribution of loss and phase shift of the feeding line of the 128 channels

Despite the loss evaluated in the simulations, the loss per unit length on the stripline presents some discrepancy with the measured value in the regular array, which is 0.12 dB/mm. For a fair comparison of the losses, the measured value is used to study the increase of losses on the feed network. The feed line length in the irregular array is 7.28 mm. This represents a 0.3 dB increase of loss per element concerning the regular array, as can be seen in Table 4.1.

Table 4.1: Loss comparison on feeding network between regular and irregular designs at 30 GHz based on measured data

| Array     | Line length | Loss per element |
|-----------|-------------|------------------|
| Regular   | 4.74 mm     | 0.57 dB          |
| Irregular | 7.28 mm     | 0.87 dB          |

## 4.2 Distribution network

Although an extra complexity on the design has been taken to equalize the lines in the feeding network, it is not feasible to do the same in the distribution network. Due to several crossings between both polarization channels, the distribution network is formed by microstrips on layer Cu-1 and striplines on layer Cu-2. As a result, each transmission line in the Wilkinson splitter network is different in terms of length but also in the number of transitions between layers.

The losses and phase shifts on the distribution lines are analyzed through simulations and the results at 30GHz are the ones shown in Figure 4.5. It has been computed from the RF connector position

until the IC RF ports (excluding the short stripline before the port equal in all ports). The line loss varies from 12.9 dB to 32.5 dB, which is compensated in the calibration of the following section.

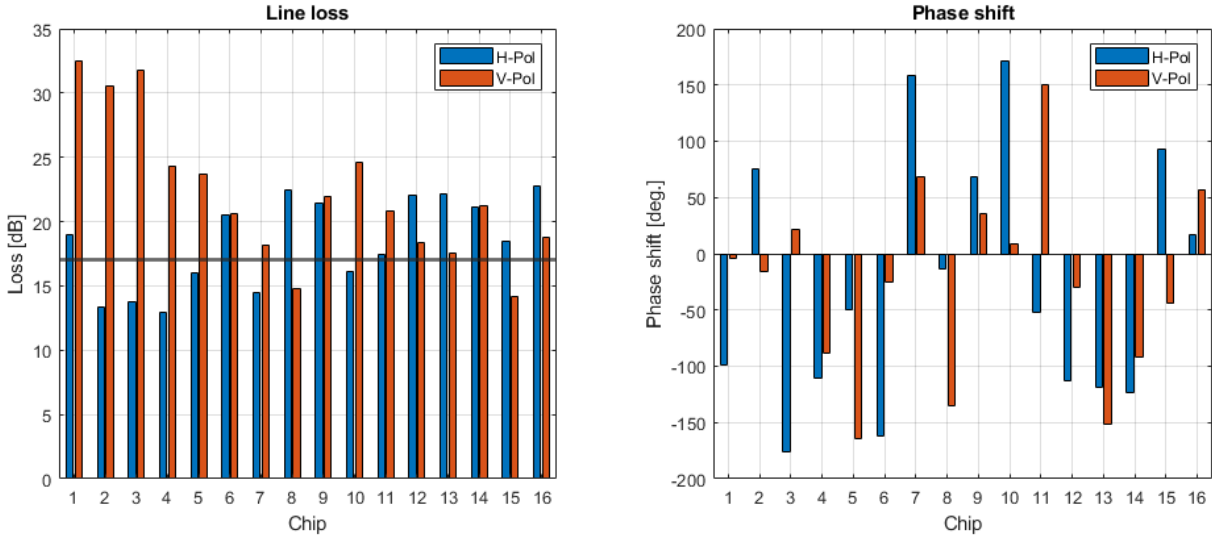


Figure 4.5: Loss and phase shift characterization of distribution lines at 30GHz of each beamformer IC

The loss on the distribution lines is also computed analytically from the measured loss per unit length of the microstrip and stripline of the previous regular design as well as the loss of each splitter. The results are shown in Figure 4.6 and compared with the line loss of the regular array, which is the black line at 17.04 dB. The loss values follow a similar trend but they do not match with the simulation results, therefore the simulation model needs to be further investigated. Compared to the regular array, the maximum loss increase is 5.44 dB and the mean is 1.91 dB above.

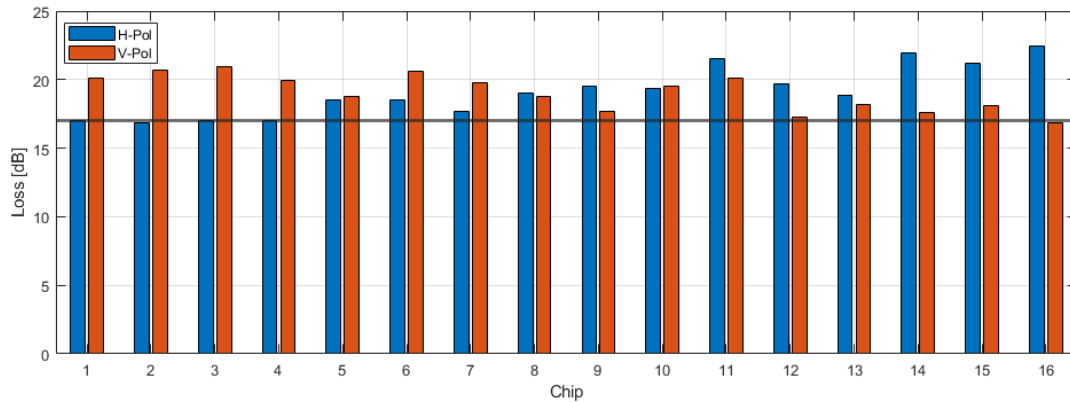


Figure 4.6: Loss of distribution lines at 30GHz from measured loss per unit length

### 4.3 Calibration approach

Based on the results from Figure 4.5 on the distribution network, the calibration in Table 4.2 is proposed such that all channels are equalized in terms of amplitude and phase shift. The numbers corresponding to each IC and its RF ports are shown in Figure 4.7.

Table 4.2: Proposed gain and phase shift values for beamformer ICs calibration

| IC / Parameter | RF 0      |              | RF 1      |              |
|----------------|-----------|--------------|-----------|--------------|
|                | Gain (dB) | Phase (deg.) | Gain (dB) | Phase (deg.) |
| 1              | 19.57     | 106.27       | 6.03      | 12.36        |
| 2              | 17.63     | 95.32        | 0.39      | -173.80      |
| 3              | 18.81     | 132.21       | 0.77      | -64.56       |
| 4              | 11.40     | 22.80        | 0.00      | 0.00         |
| 5              | 10.73     | -53.11       | 3.08      | 60.61        |
| 6              | 7.69      | 86.15        | 7.58      | -50.53       |
| 7              | 5.27      | 179.14       | 1.54      | -90.07       |
| 8              | 1.84      | -24.28       | 9.52      | 96.99        |
| 9              | 9.04      | 146.49       | 8.51      | 179.23       |
| 10             | 11.62     | 119.56       | 3.20      | -77.72       |
| 11             | 7.90      | -98.69       | 4.51      | 58.63        |
| 12             | 5.44      | 81.09        | 9.06      | -2.39        |
| 13             | 4.56      | -40.48       | 9.17      | -7.35        |
| 14             | 8.25      | 19.54        | 8.22      | -12.94       |
| 15             | 1.26      | 66.50        | 5.53      | -156.24      |
| 16             | 5.80      | 168.01       | 9.82      | 127.31       |

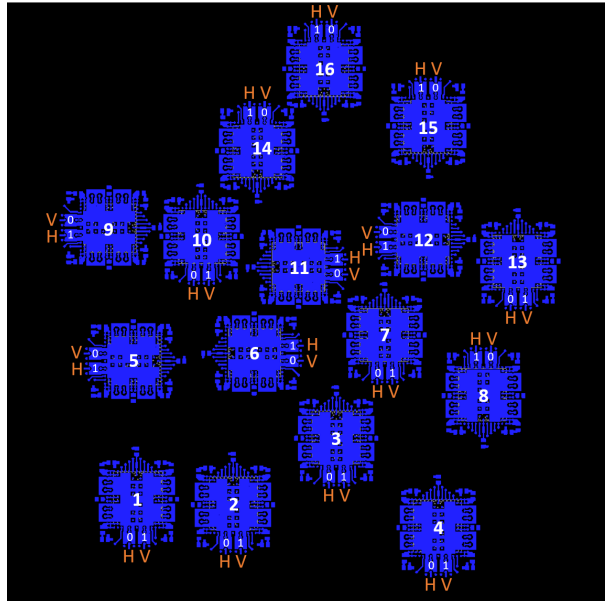


Figure 4.7: Beamformer ICs numbering and ports

## 4.4 Conclusions

From the loss analysis, the channel response of the feeding lines is computed to verify that all of them have a similar response to avoid the asymmetry effects on array scanning, which could lead to beamwidth enlargement or scanning angle deviation. The loss on the feed lines has been compared with the regular case under practical design. In addition, the distribution network is simulated to evaluate the losses on the distribution lines but also to plan the calibration for the experimental verification. Overall, the losses added on the radiated power due to the asymmetry of the layout can be considered negligible, although this is verified in the following chapter with the evaluation of the radiated power.

## Chapter 5

# Aperiodic antenna array analysis

In this section, the validation through simulation results is performed and in the future, it will be further validated and compared with experimental results. The array is analyzed in terms of resonance and radiation patterns with adaptive beamforming and also single element excitation embedded in the array. Finally, the results are compared to the regular array used as reference and others from the literature to demonstrate the improvement of using sparse irregular phased arrays in spite of the increased design complexity.

Although the array topology has been optimized with an averaged embedded element pattern measured from a similar antenna (reference panel), the mutual coupling should be checked on the new array to observe its impact on the SLL of the overall antenna. Moreover, it should also be verified that the embedded element pattern used for the optimization is similar to the current embedded element pattern. Then, the array is simulated with the antenna elements excited at the center of the coaxial at layer M6. The feeding lines are not included in the full-wave simulations although their loss is considered in the EIRP value.

### 5.1 Resonance and S-Parameters

Due to the large size of the simulation, the simulations of the antenna array have been performed only at the central frequency of 26 GHz. Therefore the resonance and performance over the entire frequency band has not been feasible yet and will be extended and also evaluated experimentally. However, at the central frequency all the channels show a reflection coefficient below -10 dB so at least at the center of the band, the antenna array shows good resonance.

### 5.2 Beamforming results

In the table below the results are shown and compared with the expected values from the feasibility study in order to verify the simulation validity and detect possible issues of the model. The first two rows represent the simulation results for both polarization, shown in Figures 5.1a and 5.1b for horizontal case. The third one is the averaged EEP from the simulation (Fig. 5.3b) multiplied by the array factor. And the last row is also the synthesized array factor but with the assumed EEP

that was initially used for the topology optimization in the feasibility study, which is the average of the measured EEP from the demo antenna (Fig. 5.3a).

After several iterations on the antenna array model, the results are substantially improved. When the beam is pointing at broadside (Fig. 5.1a), the results from the simulation are close to the targeted SLL reduction of -20 dB and achieve greatly the EIRP targeted of 56 dBm. In this case, the polarization does not have a big impact on the performance. Nonetheless, the results do not match exactly with the synthesized array factor from the averaged simulated and assumed EEP. The EIRP is less than 1 dB below the expected but the SLL differs by 3-4 dB, which sets the interference reduction below than expected.

When the array is scanning at the edge of the coverage of the base station (Fig. 5.1b), the received power is still above the desired value and the SLL is 7 to 5 dB below the aimed level (-20 dB). Nevertheless, it represents already a great enhancement as compared to the achieved performance with a regular array. When scanning at such a wide angle, the polarization of the antenna becomes an important factor. In this case, the EIRP differs up to 3.8 dB from the estimated performance. the discrepancy on SLL becomes larger at the edge of the coverage.

*Table 5.1: Beamforming results from full-wave simulations, synthesized array factor and estimated results from feasibility study*

| Array               | Broadside beam |               | Corner beam |               |
|---------------------|----------------|---------------|-------------|---------------|
|                     | EIRP (dBm)     | Max. SLL (dB) | EIRP (dBm)  | Max. SLL (dB) |
| Simulated H-Pol     | 61.19          | -19.75        | 57.77       | -15.31        |
| Simulated V-Pol     | 61.24          | -19.03        | 56.86       | -13.23        |
| AF w/ simulated EEP | 61.89          | -23.44        | 58.24       | -16.90        |
| AF w/ assumed EEP   | 61.7           | -22.5         | 60.7        | -20.2         |

The same simulation and comparison have been performed on the regular (Fig. 5.1c-5.1d) array in order to evaluate and confirm the enhancement through simulations before the manufacturing. As seen in Table 5.2, the EIRP value difference between the simulated and estimated results is very similar to the one of the irregular array in Table 5.1. The SLL is increased by around 1 dB with respect to the estimated value at broadside, probably due to the difference of EEP assumed and simulated. However, it should be noted that the simulation results from the first two rows match with the third row, which means that the EEP is more uniform over all the elements in the regular array than in the irregular case. Therefore, this should be improved in future iterations of the design, by for example adding dummy elements. When the beam is pointing at the corner, the SLL is slightly reduced by 1 dB from the expected value with H-pol. and by 2 dB with V-pol., probably due to the narrow EEP with vertical polarization and the wide scanning angle of the array.

The difference in performance among the rows in the above tables is believed to be caused by the discrepancy of the EEP. First of all, the pattern is different for horizontal and vertical polarization, being degraded in the vertical case due to the wide scanning horizontal angle of the sector cell. Regarding the difference between the simulation results and the array factor with the averaged EEP, it can be explained by two reasons. Firstly, the averaged EEP includes both polarizations which leads to a more symmetrical EEP. Secondly, due to the non-regular grid of the antenna elements and especially on the edge elements, the embedded pattern is not the same at all the elements so the averaged one does not represent all the elements in the array. And finally, the

Table 5.2: Beamforming results from full-wave simulations, synthesized array factor and estimated results from feasibility study of the regular array

| Array               | Broadside beam |               | Corner beam |               |
|---------------------|----------------|---------------|-------------|---------------|
|                     | EIRP (dBm)     | Max. SLL (dB) | EIRP (dBm)  | Max. SLL (dB) |
| Simulated H-Pol     | 60.83          | -13.89        | 57.41       | -9.66         |
| Simulated V-Pol     | 60.76          | -13.42        | 57.00       | -8.52         |
| AF w/ simulated EEP | 61.29          | -13.41        | 58.23       | -9.84         |
| AF w/ assumed EEP   | 61.0           | -12.5         | 60.5        | -10.6         |

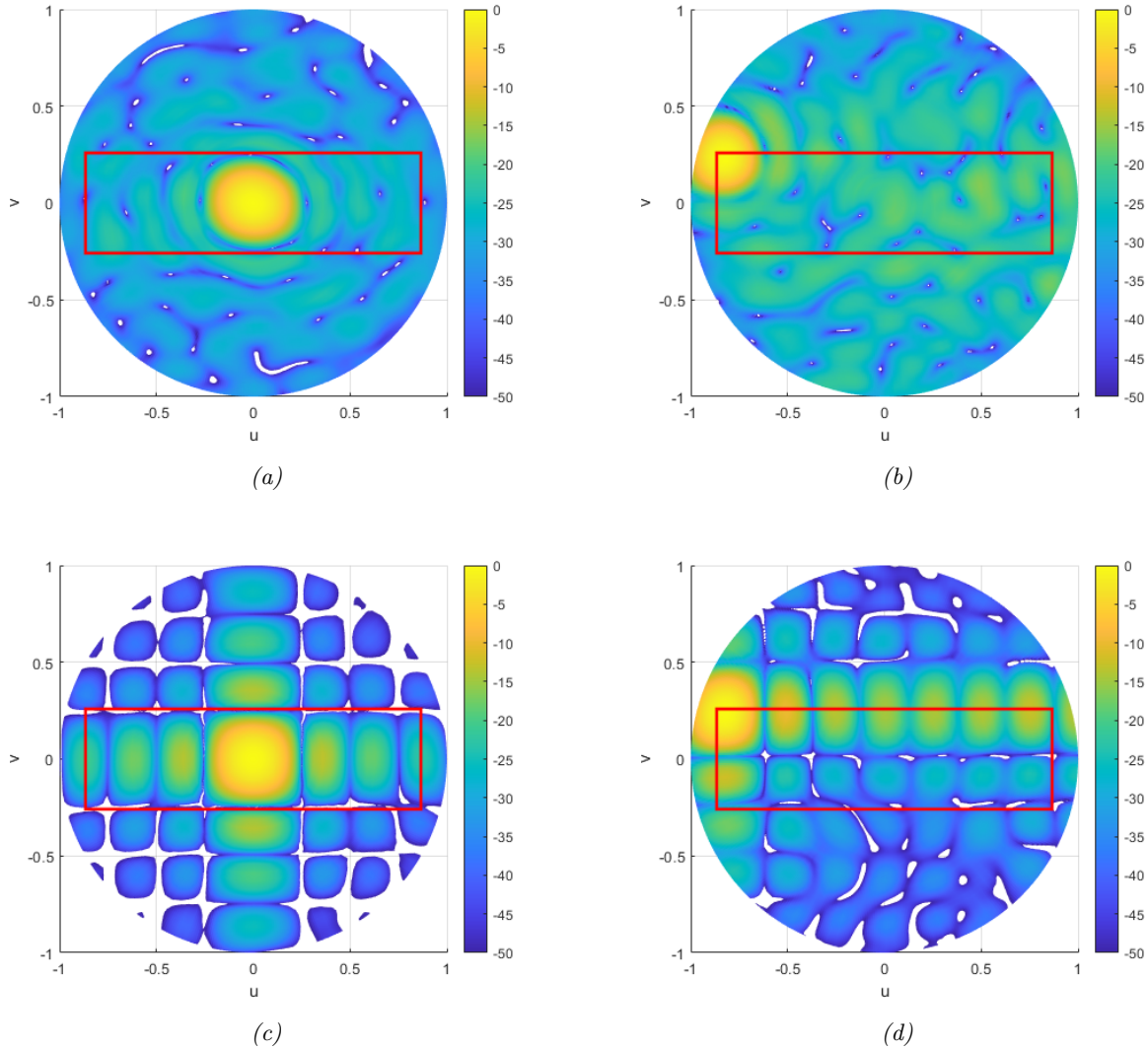


Figure 5.1: Normalized radiation pattern with H-Pol. Beam (a) at broadside and (b) at EoC with irregular array and (c) at broadside and (d) at EoC with regular array (sector coverage limited with the rectangle:  $\pm 60$  deg. in azimuth and  $\pm 15$  deg. in elevation.)

last two rows in Table 5.1 do not correspond because the assumed EEP used for the layout array topology optimization is not the same as the one resulting from the simulations on the irregular array. This is explained and analyzed further in the following section.

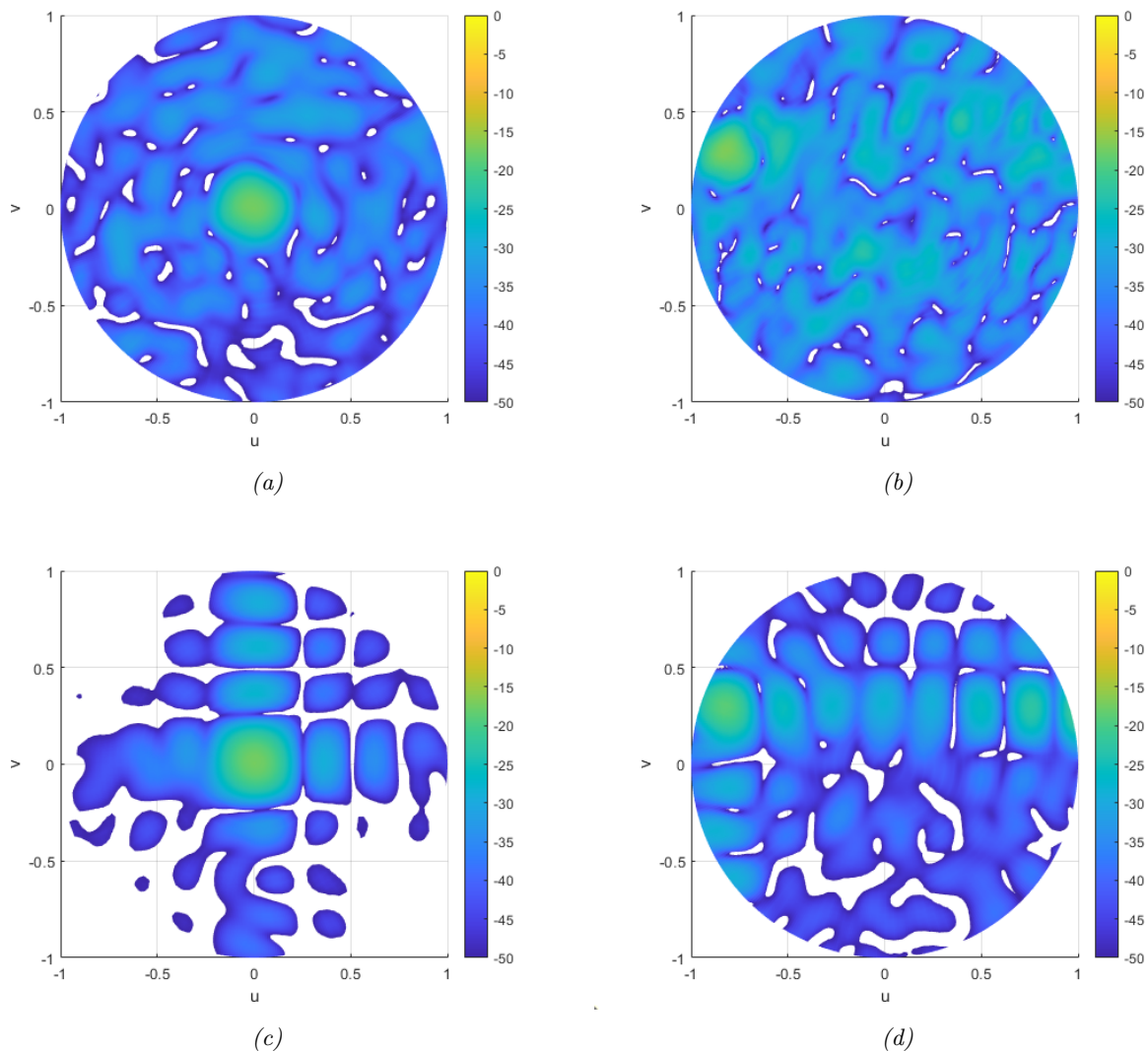


Figure 5.2: Normalized cross-pol. radiation pattern with respect to the maximum value of co-pol. at each scanning angle with H-Pol. Beam (a) at broadside and (b) at EoC with irregular array and (c) at broadside and (d) at EoC with regular array

The cross-polarization of the adaptive beamforming (Fig. 5.2) is also evaluated to validate the decoupling between both polarizations. As can be seen in Table 5.3, the cross-polarization varies strongly with the beam position. The average of maximum values with respect to the co-polarization maximum over several scanning angles along the sector window is -15.7 dB on average, which is improved by around 1 dB as compared with the reference array, where the average along the sector window is -14.8 dB. The cross-pol. is lower than -10 dB in most of the angles. When pointing at  $\pm 60$  deg., it is higher when using vertical polarization, which in the worst case is -4.29 dB

with respect to the maximum co-polarization directivity. This is caused by the narrow embedded element pattern in the vertical case, explained in the following section. In all cases, the maximum of cross-polarization and co-polarization coincides.

Table 5.3: Maximum value of cross-polarization normalized with respect to maximum of co-polarization of each scan beam

| Beam position  | Max. Cross-pol (dB) |          |
|----------------|---------------------|----------|
|                | Horizontal          | Vertical |
| Broadside beam | -17.3               | -17.11   |
| Corner beam 1  | -14.45              | -14.37   |
| Corner beam 2  | -17.71              | -7.02    |
| Corner beam 3  | -10.14              | -4.29    |
| Corner beam 4  | -16.66              | -13.97   |
| Side beam 1    | -22.53              | -16.27   |
| Side beam 2    | -15.07              | -6.07    |
| Side beam 3    | -19.59              | -17.81   |
| Side beam 4    | -15.19              | -17.34   |

### 5.3 Embedded element pattern

The main reason for the beamforming results not being as good as expected remains on the embedded element pattern of the antenna. First of all, the EEP used for the array topology optimization was the average of the measured EEP from the demo antenna (Figure 5.3a). Due to antenna element modifications and the non-uniform element placing of the array, the EEP obtained from the irregular array is quite different. Moreover, the regular array uses a sequential rotation to symmetrize the EEP which is not applied to the irregular layout. The new EEP in Figure 5.3b shows a different pattern that creates a discrepancy between the last two rows of Table 5.1.

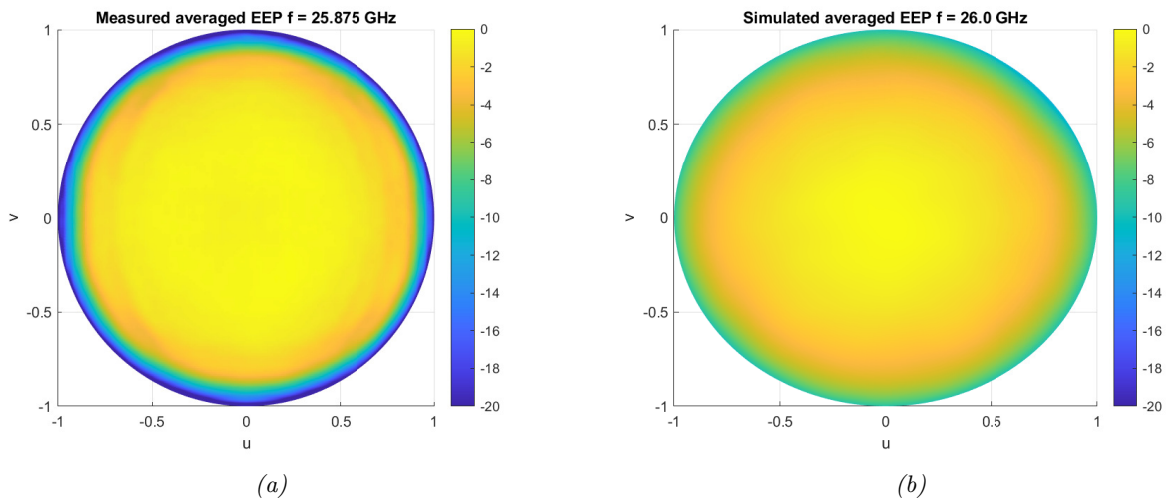


Figure 5.3: Averaged embedded element patterns from (a) measurements and (b) simulation results

Secondly, the radiation pattern changes dramatically between horizontal and vertical polarization as can be seen in Figure 5.4. The radiation is more intense along the axis corresponding to the excited polarization. Since the sector cell is wider horizontally than vertically (60 deg. in azimuth by 15 deg. in elevation), the performance on the azimuth extremes ( $\pm 60$  deg.) is degraded with the vertical polarization. This can be seen in Figure 5.6 where the sidelobe level is much better with horizontal polarization on the beam positions from 2 to 7, which correspond to the beams pointing at  $\pm 60$  deg. azimuth.

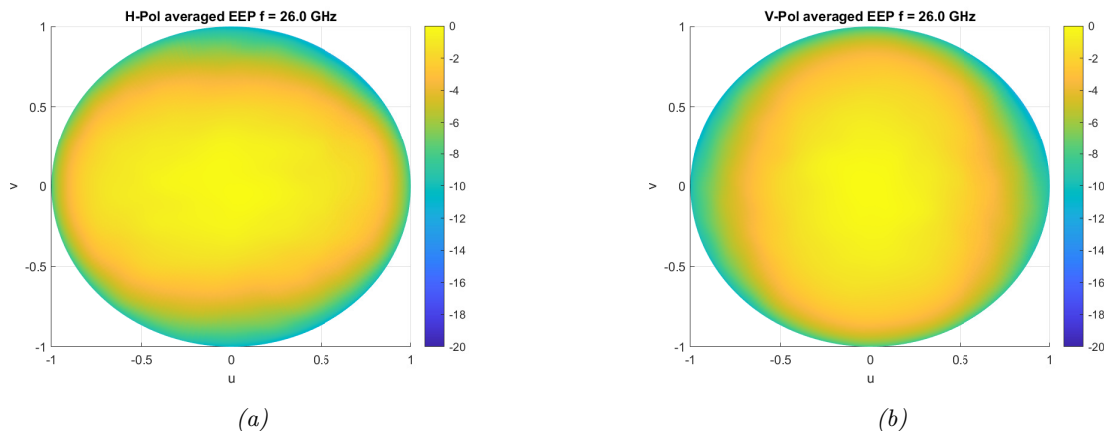


Figure 5.4: Averaged embedded element patterns from simulation results for (a) horizontal and (b) vertical polarization

These problems are addressed in Section 3.8 for recommended improvements in future designs. A co-optimization of the layout topology could be done using each EEP from both polarization, to avoid scanning degradation in one of them when using dual-pol arrays. Also, the antenna element could be different to reduce polarization dependence on the element pattern.

## 5.4 Comparison with a regular array

In order to easily compare the improvement with respect the array with a regular layout, the EIRP and SLL values obtained through the simulations are presented in Figures 5.7 and 5.6 for both irregular and regular array excited with uniform and non-uniform amplitude tapering. The irregular array is evaluated with uniform (Fig. 5.5a) and 1-step amplitude tapering (Fig. 5.5b). The regular array uniform (Fig. 5.5c) and Chebyshev window of 17 dB (Fig. 5.5c) since it gives a similar interference cancellation as the designed irregular array. The corresponding beam positions of the x-axis are shown in Figure 5.8.

The major improvement of the uniform-tapered sparse layout is the reduction of interference while keeping a good power level at the receiver. The sidelobe level is improved by 5.61 dB to 8.36 dB while the maximum EIRP degradation is 0.79 dB, although in most cases the EIRP is improved with respect to the regular array. If the interference level needs to be further improved, the sparse array with non-uniform tapering can achieve up to 9.93 dB of SLL reduction with respect to the regular array. Therefore, the maximum SLL can be reduced up to -22 dB. However, the power efficiency is degraded due to the tapering, with a maximum of 2.86 dB of EIRP reduction.

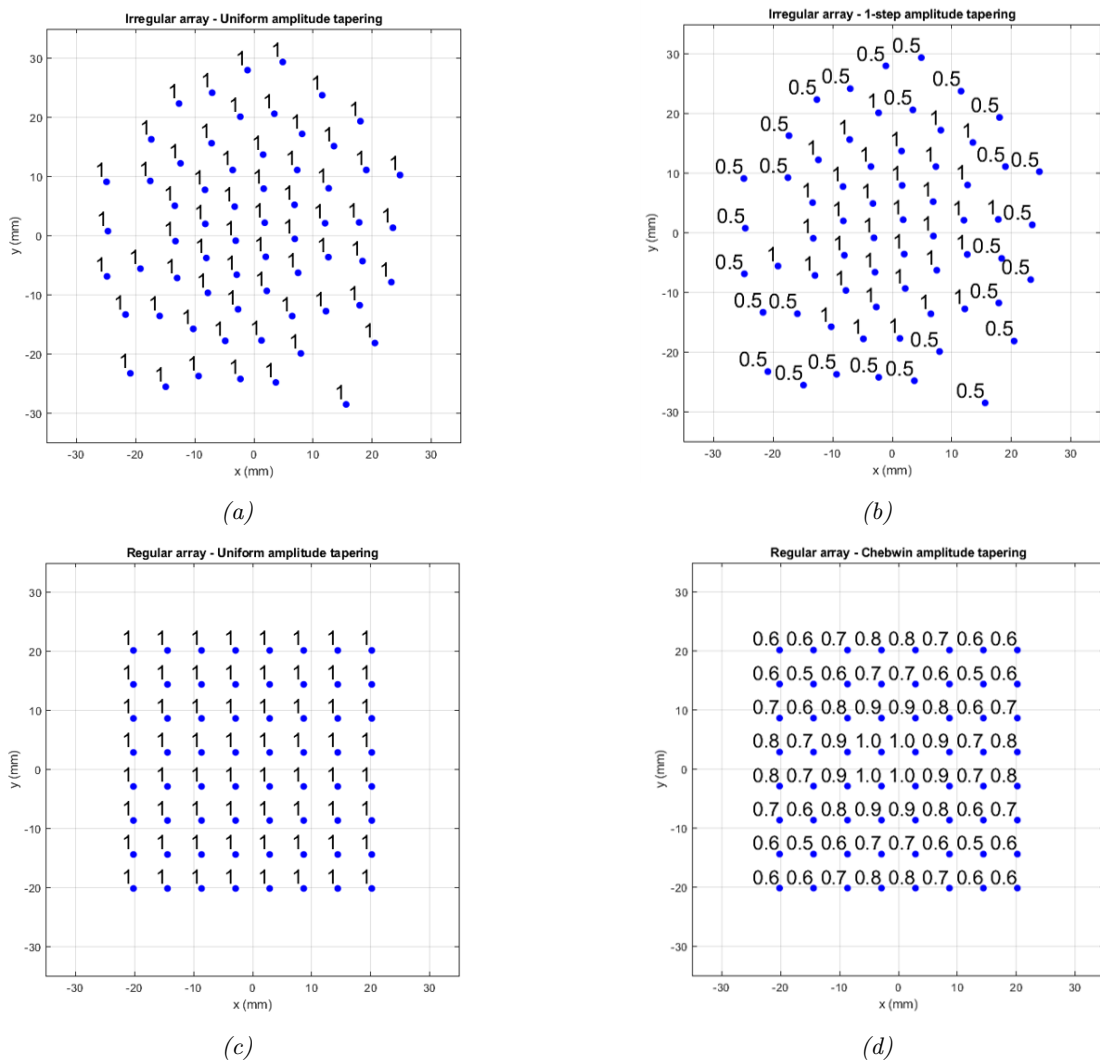


Figure 5.5: Amplitude tapering on irregular array: (a) uniform and (b) 1-step amplitude tapering; and on regular array (a) uniform and (b) Chebyshev window

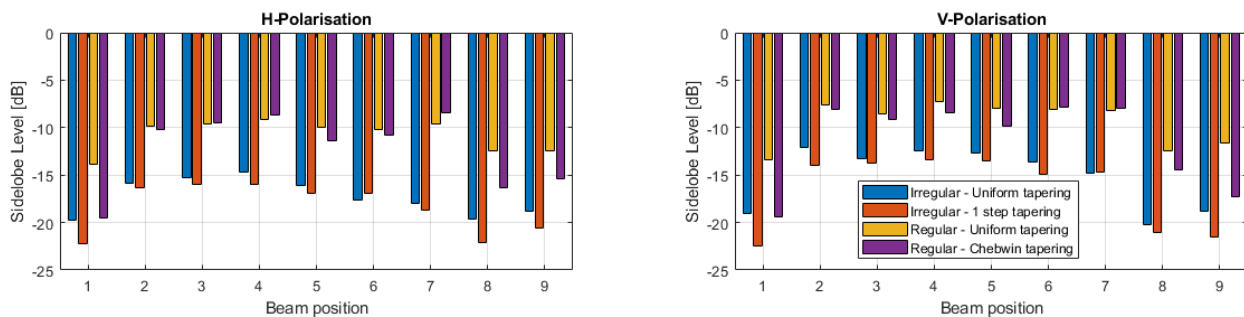


Figure 5.6: Performance comparison in terms of Side Lobe Level

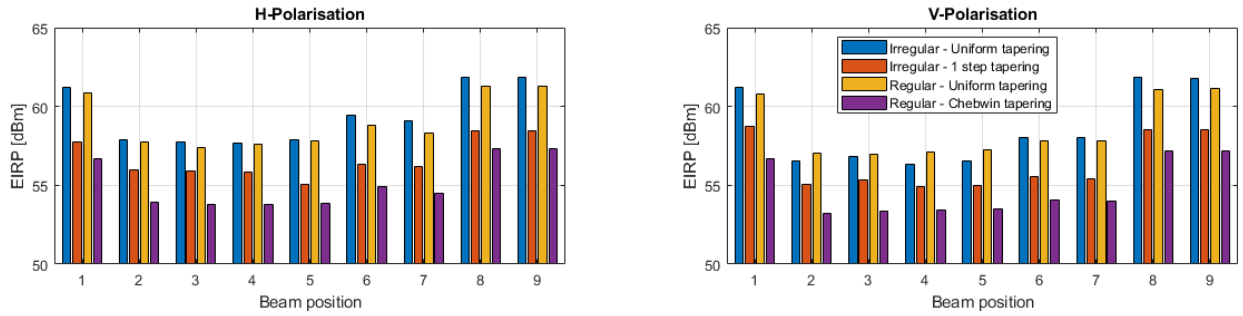


Figure 5.7: Performance comparison in terms of EIRP

In the figures above, the regular array is also tapered to reduce interference that can achieve a maximum SLL of almost -20 dB at broadside and some improvement on the beams close to broadside, but small improvement or none is seen when scanning at wider angles. Besides the lower improvement on SLL with respect to the irregular array, the EIRP degradation is a huge problem. On average, the EIRP value with the Chebyshev window is 4 dB and 1.6 dB below the EIRP of the irregular array with uniform and non-uniform, respectively. Therefore, the superior performance of the irregular array is demonstrated with a better EIRP and SLL trade-off that cannot be achieved with the regular array.

Table 5.4: Antenna performance comparison at broadside

| Topology  | Amplitude tapering | Beamwidth (deg.) | Directivity (dBi) | EIRP (dBm) | Max. SLL (dB) |
|-----------|--------------------|------------------|-------------------|------------|---------------|
| Irregular | Uniform            | 11.52            | 24.00             | 57.86      | -19.75        |
| Irregular | 1-step tapering    | 14.76            | 22.3              | 57.76      | -22.26        |
| Regular   | Uniform            | 12.60            | 23.34             | 57.76      | -13.89        |
| Regular   | Chebyshev 17dB     | 14.40            | 22.39             | 53.90      | -19.55        |

Table 5.5: Antenna performance comparison at the edge of coverage

| Topology  | Amplitude tapering | Beamwidth (deg.) | Directivity (dBi) | EIRP (dBm) | Max. SLL (dB) |
|-----------|--------------------|------------------|-------------------|------------|---------------|
| Irregular | Uniform            | 22.50            | 20.73             | 57.92      | -16.12        |
| Irregular | 1-step tapering    | 26.10            | 19.63             | 55.09      | -16.87        |
| Regular   | Uniform            | 23.22            | 20.32             | 57.81      | -10.00        |
| Regular   | Chebyshev 17dB     | 25.74            | 19.58             | 53.87      | -11.43        |

In Tables 5.4 and 5.5 a more in depth comparison is done including other meaningful parameters to evaluate the antenna performance besides EIRP and SLL, such as beamwidth and directivity. The radiation pattern for both uniform irregular and regular cases is shown in Figure 5.1. The considered arrays and amplitude tapering are the same as in the previous comparison evaluated at broadside and at the edge of the coverage.

The regular array using the Chebyshev tapering achieves almost -20 dB of maximum SLL at broadside as the irregular layout with uniform tapering, but the power efficiency is reduced with an EIRP

about 4 dB lower than the other cases. The beamwidth is wider leading to a lower directivity by about 1.6 dB. Similarly, at the edge of the coverage in Table 5.5, the same parameters are degraded by similar values although the maximum SLL cannot be more reduced than -12 dB.

Therefore, the irregular array using uniform amplitude tapering demonstrates the capacity of canceling interference by almost 6 dB with high power efficiency and better beamwidth and directivity than the regular array can achieve. In case the interference needs to be further minimized, a maximum SLL of -22 dB is possible by applying amplitude tapering. Although the power efficiency is degraded, the EIRP at broadside is only decreased by 0.1dB and less than 3 dB at EoC.

Table 5.6: A performance comparison of several state-of-the-art active phased array antenna systems with the aperiodic phased array designed

| Array  | UCSD [19]                                 | IBM [20]                                     | Nokia Bell Labs [21]                            | Qualcomm [22]   | This work                       |
|--|---|--|---|---|---------------------------------|
| Number of elements                               | 8x8                                       | 10x10 with two outer rings of dummy elements | 8x8   | 8x32 with two rows and four columns of dummy elements | 64 in irregular grid            |
| Transmit/receive beamformer chips                | 16  | 4  | 16  | 32  | 16                              |
| Central frequency (GHz)                          | 30  | 28   | 28  | 28  | 26                              |
| Antenna element type                             | Stacked patch antennas                    | Aperture coupled patch                       | Capacitively coupled patch                      | Patch antennas  | Stacked patch antennas          |
| Antenna array layout                             | Square grid $0.5\lambda$ by $0.63\lambda$ | Square grid $0.5\lambda$ spaced              | Equilateral triangular grid $0.5\lambda$ spaced | Square grid total active aperture of 160mm by 40mm    | Square grid $0.5\lambda$ spaced |
| Polarization                                     | Single                                    | Dual   | Single  | Dual  | Dual                            |
| EIRP (dBm) at broadside                          | 52  | 54   | 48  | 64  | 61                              |
| Max. SLL (dB) for a beam at broadside            | -12                                       | -13  | -13   | -10   | -19.75                          |
| Max. SLL (dB) for a beam at EoC                  | -10                                       | -10  | -10   | -8  | -16.12                          |
| Reference scan range (deg.) in elevation/azimuth | $\pm 25 / \pm 50$                         | $\pm 50 / \pm 50$                            | $\pm 45 / \pm 45$                               | $\pm 50 / \pm 50$                                     | $\pm 15 / \pm 60$               |

The simulation results of the uniform-tapered irregular array are compared in Table 5.6 with the state-of-the-art phased arrays presented in the first chapter (Table 1.1) although their performance is based on experimental data. The maximum sidelobe level from the arrays taken from the literature is -10 to -13 dB pointing at broadside and -8 to -10 dB at the edge of coverage. With the new irregular array, the full-wave simulation outputs demonstrate a maximum SLL of -19.75 dB at broadside and -16.12 at the edge of coverage. That means an improvement up to 9.75 dB and 8.12 dB at broadside and corner scanning, respectively.

## 5.5 Conclusions

The validation through full-wave simulations shows positive results suggesting that it is a good idea to proceed with the realization and experimental verification of the aperiodic antenna array. The reflection coefficient at the center frequency indicates good resonance taking into account the coupling effect in the array, although the parameter should be checked over the frequency band of the antenna. Despite the fact that the beamforming and scanning capabilities are below the estimated values during the feasibility study, the improvement with respect to the regular arrays is very meaningful. The interference cancellation is improved by 5.6 to 8.36 dB while keeping an even better EIRP in some cases, which can be further improved up to -10 dB reduction using amplitude tapering. From analyzing the embedded element pattern, the discrepancies with the estimated performance are explained and a couple of improvements from section 3.8 are recommended in order to mitigate those discrepancies and improve the overall performance.

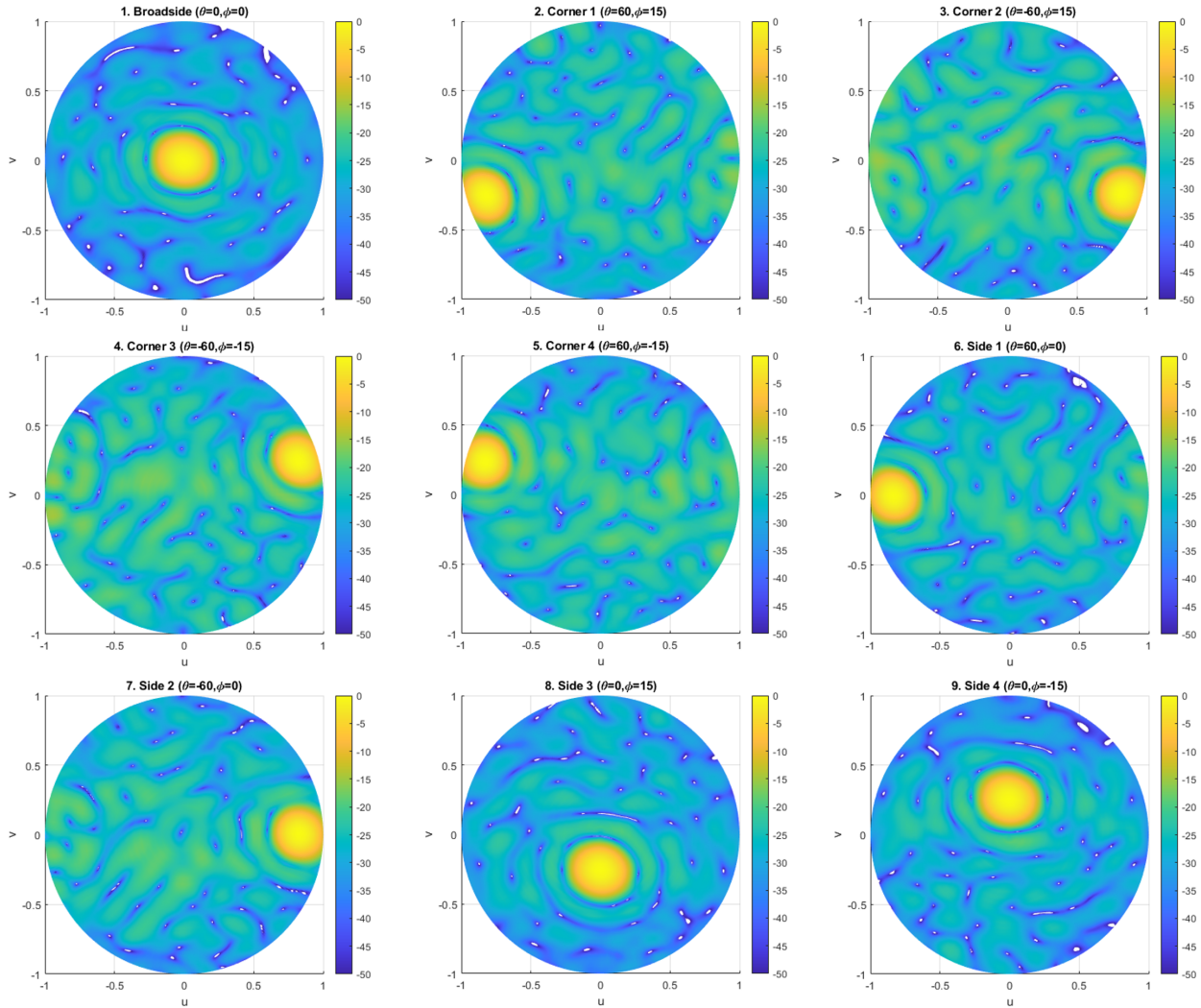


Figure 5.8: Beam scanning positions used for analysis of the results (broadside, corners and center of the side of the sector cell)

## Chapter 6

# Conclusions and future work

In this last chapter, the conclusions from this project are drawn and its novelties and impact on current base stations are stated. Furthermore, some future lines are recommended to continue with the validation of the current array design and to improve the array in future design iterations.

### 6.1 Conclusions

In this thesis, the next-generation base station antenna array design has been discussed with a focus on the multi-user scenarios in which several users share the same time-frequency resource blocks for spectral efficiency. To guarantee high quality of service and fairness among all users, it is essential to have a low sidelobe level to prevent users from suffering from high interference levels. Therefore, it is very important to minimize the maximum sidelobe level at the base stations. However, the current work on phased arrays for mm-wave base stations uses uniformly-fed regular layouts with half-wavelength spacing, which can offer a maximum SLL of about -13 dB.

To satisfy these challenges demands, an alternative to the current state-of-the-art concept for the antenna array - aperiodic arrays - has been recently proposed. In this thesis, a novel completely aperiodic active antenna array has been designed and its performance has been verified against conventional regular antenna array by means of full-wave simulations. The loss analysis on the feeding lines was also within the scope of the thesis to evaluate fairly the benefits and drawbacks of using irregular layout topology. The results are positive and show a valuable improvement, which leads the project to the manufacturing stage for the experimental verification of the design.

The initial phase of the design was focused on the feasibility study for the array topology selection to achieve the targeted performance: minimizing the SLL as much as possible while maintaining a similar or even better EIRP as compared to the regular reference array. Besides the antenna characteristics, the selection process was also under another criterion to minimize the increase of losses in the feeding lines due to its irregularity. For that, novel design constraints on chip placement and line length equalization are presented and later applied in the design process.

Using the regular array as a baseline design, the design process has been focused on overcoming the challenges introduced by the aperiodic structure, such as minimizing the losses by optimally placing the chips and routing the equalized feeding lines to avoid the calibration process. The antenna

tuning and isolation to minimize mutual coupling have also been a meaningful part of the process. By designing and integrating all the blocks of the antenna panel, the design of the aperiodic phased antenna array system is completed.

In the loss analysis, the loss in the transmission lines has been evaluated and compared between the regular and irregular networks under practical design. In the feeding network, there is a loss increase of 0.3 dB per element, which can be considered a negligible drawback thanks to the high power efficiency of the array, resulting in a high EIRP on the base station. In the case of the distribution network, it varies in each line due to the different lengths and the mean loss increase is less than 2 dB. Although in some cases the loss is significantly higher, it does not degrade the power efficiency of the array since it can be compensated with the gain of the power amplifier at the beamformer IC.

From the antenna array characteristics evaluation, a meaningful improvement on interference cancellation with high power efficiency sets aperiodic arrays as a promising approach for mm-wave base stations. A reduction of around 6 dB on the sidelobe level can be achieved with a similar EIRP in comparison to the regular array, which is almost -20 dB of the maximum sidelobe level. Beamwidth, directivity, and cross-polarization maxima parameters of the irregular array are slightly improved when compared to the regular one. If amplitude tapering is applied, the interference can be reduced even further, almost an improvement of 10 dB in some cases (leading to a maximum SLL of -22 dB), with a small degradation on the received power lower than 3 dB, which is an extraordinary trade-off.

Overall, it can be concluded that the design challenges added due to irregularity are worth dealing with due to the high interference reduction achieved. After finalizing the first-time design of an irregular feed network with multi-channel mm-wave beamformer chips, the losses for regular and irregular networks under practical design criteria have been compared for the first time. The additional losses on the irregular network can be considered negligible taking into account the advantages in antenna performance. Therefore, the aperiodic sparse array concept is shown to be a viable and promising option for the next generation of mm-wave base station antennas.

The aperture size is increased by 43.5% with respect to the reference array and the design of the complete antenna array has been more challenging due to its irregularity. However, the achievable level of interference reduction among users with such aperiodic phased antenna arrays supposes a great achievement because it does not degrade other aspects of the array performance as beamwidth, directivity, or power efficiency without increasing the complexity in the MAC layer. From the comparison of the array with the state-of-the-art active phased array antenna systems, the interference cancellation can be improved by almost 7 dB.

By deploying aperiodic phased arrays - synthesized by such a multi-disciplinary layout optimization algorithm - in mm-wave base stations of 5G and beyond, the interference level among users within the coverage can be reduced sufficiently such that the spectral efficiency and service quality achieved are significantly improved.

## 6.2 Future work

Some future lines can be drawn to continue the research on this topic. First of all, the realization of the designed prototype for the experimental verification and comparison of the results is an important task to validate the design and the simulation results. The current analysis should be extended from a single frequency to a certain frequency band for complete validation of the array response at all the frequencies of interest.

Another interesting task would be to improve the array design to address the issues already detected during the validation. These are mainly due to non-uniform EEP among the antenna elements and their dependence on polarization. A couple of solutions are proposed, detailed, and analyzed in this thesis to deal with them. One is to improve the topology optimization process for a sub-optimal topology suitable for both polarizations and the other one is to apply sequential mirroring on the feeding lines for a more symmetrical pattern and wider band operation. In addition, the design of a different array element could be a potential improvement to control the antenna element patterns.

## 6.3 Publications

A paper is being prepared to submit to the IEEE Communications Magazine in a near future. Future publications to other journals are expected, particularly after the experimental validation of the array.



# Bibliography

- [1] Y. Aslan, “Antenna array synthesis and beamforming for 5G applications: An interdisciplinary approach,” Ph.D. dissertation, TU Delft, August 2020.
- [2] P. Hindle, J. Madden, M. Kappes, C. Bencivenni, T. Emanuelsson, M. Gustafsson, D. Sikri, and R. M. Jayasuriya, “5G phased array technologies,” *Microwave Journal*, 2019.
- [3] A. Osseiran, S. Parkvall, P. Persson, A. Zaidi, S. Magnusson, and K. Balachandran, “5G radio access: An overview,” *Ericsson Review*, 2014.
- [4] *6G: The Hyper-Connected Experience for All*, Samsung Research, 2020.
- [5] D. Warren and C. Dewar, “The 5G guide: A reference for operators,” *GSMA Intelligence*, 2019.
- [6] —, “Understanding 5G: Perspectives on future technological advancements in mobile,” *GSMA Intelligence*, 2014.
- [7] Samsung, “Welcome to the 5G era,” <https://www.samsung.com/semiconductor/solutions/topics/5g/>, Accessed on 25.10.2020.
- [8] R&D Highlights, Mitsubishi Electric, “Massive-element antenna systems technology for 5G base stations,” <https://www.mitsubishielectric.com/en/about/rd/research/highlights/communications/5g.html>, 2017, Accessed on 22.10.2020.
- [9] F. A. Dicandia and S. Genovesi, “Exploitation of triangular lattice arrays for improved spectral efficiency in massive MIMO 5G systems,” *IEEE Access*, vol. 9, pp. 17 530–17 543, 2021.
- [10] Y. Aslan, J. Puskely, A. Roederer, and A. Yarovoy, “Trade-offs between the quality of service, computational cost and cooling complexity in interference-dominated multi-user sdma systems,” *IET Comm.*, vol. 14, no. 1, pp. 144–151, 2020.
- [11] P. Angeletti and R. De Gaudenzi, “A pragmatic approach to massive MIMO for broadband communication satellites,” *IEEE Access*, vol. 8, pp. 132 212–132 236, 2020.
- [12] Y. Aslan, A. Roederer, and A. Yarovoy, “System impacts of user scheduling with minimal angular separation constraints in radio resource management for 5G and beyond,” in *2020 IEEE Asia-Pacific Microwave Conference (APMC)*, 2020, pp. 724–726.
- [13] —, “System advantages of using large-scale aperiodic array topologies in future mm-wave 5G/6G base stations: An interdisciplinary look,” *IEEE Systems Journal*, pp. 1–10, 2021.

- 
- [14] Y. Aslan, J. Puskely, A. Roederer, and A. Yarovoy, "Multiple beam synthesis of passively cooled 5G planar arrays using convex optimization," *IEEE Transactions on Antennas and Propagation*, vol. 68, no. 5, pp. 3557–3566, 2020.
- [15] X. Gu, D. Liu, and B. Sadhu, "Packaging and antenna integration for silicon-based millimeter-wave phased arrays: 5G and beyond," *IEEE Journal of Microwaves*, vol. 1, no. 1, pp. 123–134, 2021.
- [16] B. Sadhu, "Enabling 5G: mmWave silicon integration and packaging," *IBM Research*, 2015.
- [17] W. Hong, *Millimeter-Wave Antennas and Arrays*, Handbook of Antenna Technologies, Springer, Singapore, 2016.
- [18] W. Hong, K.-h. Baek, and A. Goudelev, "Grid assembly-free 60-GHz antenna module embedded in FR-4 transceiver carrier board," *IEEE Transactions on Antennas and Propagation*, vol. 61, no. 4, pp. 1573–1580, 2013.
- [19] K. Kibaroglu, M. Sayginer, T. Phelps, and G. M. Rebeiz, "A 64-element 28-GHz phased-array transceiver with 52-dBm EIRP and 8–12-Gb/s 5G link at 300 meters without any calibration," *IEEE Transactions on Microwave Theory and Techniques*, vol. 66, no. 12, pp. 5796–5811, 2018.
- [20] X. Gu, B. Sadhu, D. Liu, C. Baks, and A. Valdes-Garcia, "Antenna-in-package design and module integration for millimeter-wave communication and 5G," in *2018 International Symposium on VLSI Design, Automation and Test (VLSI-DAT)*, 2018, pp. 1–2.
- [21] R. Valkonen, "Compact 28-GHz phased array antenna for 5G access," in *2018 IEEE/MTT-S International Microwave Symposium - IMS*, 2018, pp. 1334–1337.
- [22] J. Dunworth, B.-H. Ku, Y.-C. Ou, D. Lu, P. Mouat, A. Homayoun, K. Chakraborty, A. Arnett, G. Liu, T. Segoria, J. Lerdworatawee, J. W. Park, H.-C. Park, H. Hedayati, A. Tassoudji, K. Douglas, and V. Aparin, "28GHz phased array transceiver in 28nm bulk CMOS for 5G prototype user equipment and base stations," in *2018 IEEE/MTT-S International Microwave Symposium - IMS*, 2018, pp. 1330–1333.
- [23] E. Degirmenc, "EMF test report: Ericsson AIR 5121," *Ericsson AB, Sweden*, vol. GFTB-17:001589 Uen, Rev B, 2018.
- [24] Y. Aslan, J. Puskely, J. H. J. Janssen, M. Geurts, A. Roederer, and A. Yarovoy, "Thermal-aware synthesis of 5G base station antenna arrays: An overview and a sparsity-based approach," *IEEE Access*, vol. 6, pp. 58 868–58 882, 2018.
- [25] ELKI Data Mining, "Same-size k-means variation tutorial," [https://elki-project.github.io/tutorial/same-size\\_k\\_means](https://elki-project.github.io/tutorial/same-size_k_means), Accessed on 5.11.2020.
- [26] T. Marinović, D. I. L. De Villiers, D. J. Bekers, M. N. Johansson, A. Stjernman, R. Maaskant, and G. A. E. Vandenbosch, "Fast characterization of mutually coupled array antennas using isolated antenna far-field data," *IEEE Transactions on Antennas and Propagation*, vol. 69, no. 1, pp. 206–218, 2021.
- [27] T. Teshirogi, M. Tanaka and W. Chujo, "Wideband circularly polarized array antenna with sequential rotations and phase shifts of elements," *International Symposium on Antennas and Propagation (ISAP85)*, Tokyo, 1985.

- 
- [28] A. J. van den Biggelaar, “Over-the-air characterization of millimeter-wave integrated antenna systems,” Ph.D. dissertation, Technische Universiteit Eindhoven, November 2020.
- [29] ARSI, LLC, “Using sequential rotation,” <https://arsiconsultants.com/2018/08/24/using-sequential-rotation/>, August 2018, Accessed on 15.5.2021.
- [30] T. J. Roupael, “Chapter 4 - system nonlinearity,” in *Wireless Receiver Architectures and Design*, T. J. Roupael, Ed. Boston: Academic Press, 2014, pp. 179–261, Accessed on 4.6.2021. [Online]. Available: <https://www.sciencedirect.com/science/article/pii/B9780123786401000044>
- [31] Y. Li, J. Lopez, R. Wu, and D. Y. C. Lie, “A fully monolithic bimos envelope-tracking power amplifier with on-chip transformer for broadband wireless applications,” *IEEE Microwave and Wireless Components Letters*, vol. 22, no. 6, pp. 288–290, 2012.
- [32] S. P. Yadav and S. C. Bera, “Nonlinearity effect of power amplifiers in wireless communication systems,” in *2014 International Conference on Electronics, Communication and Computational Engineering (ICECCE)*, 2014, pp. 12–17.
- [33] A. Singh and H. Kaur, “Non linearity analysis of high power amplifier in ofdm system,” in *International Journal of Computer Applications (0975 – 8887)*, vol. 37, no. 2, 2012.



## Appendix A

### Panel layout

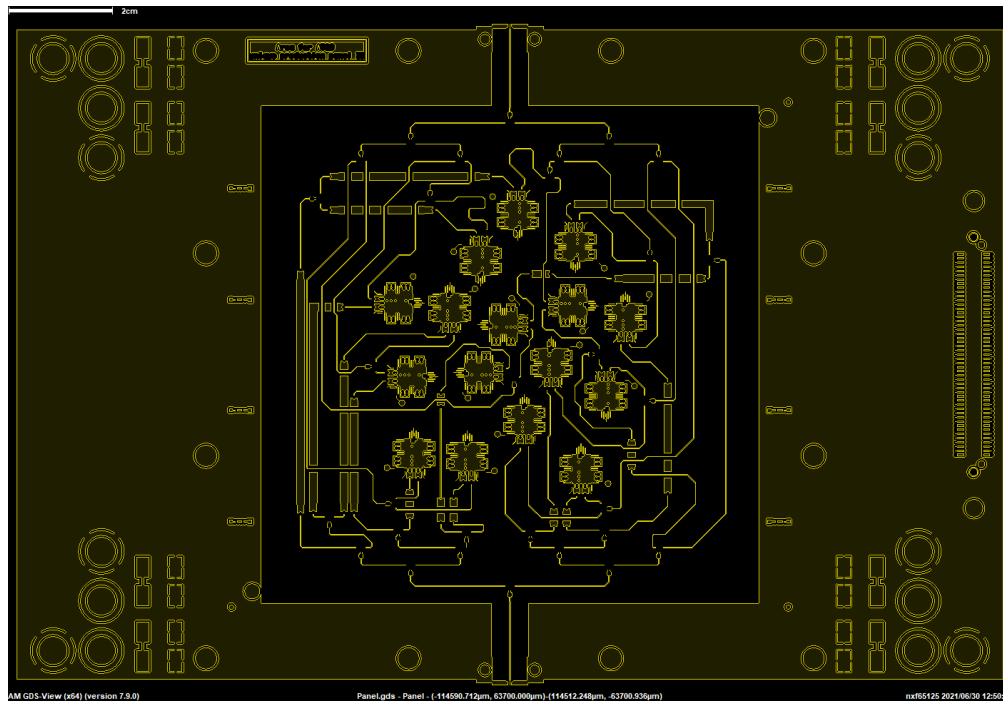


Figure A.1: Panel top view - Layer 1

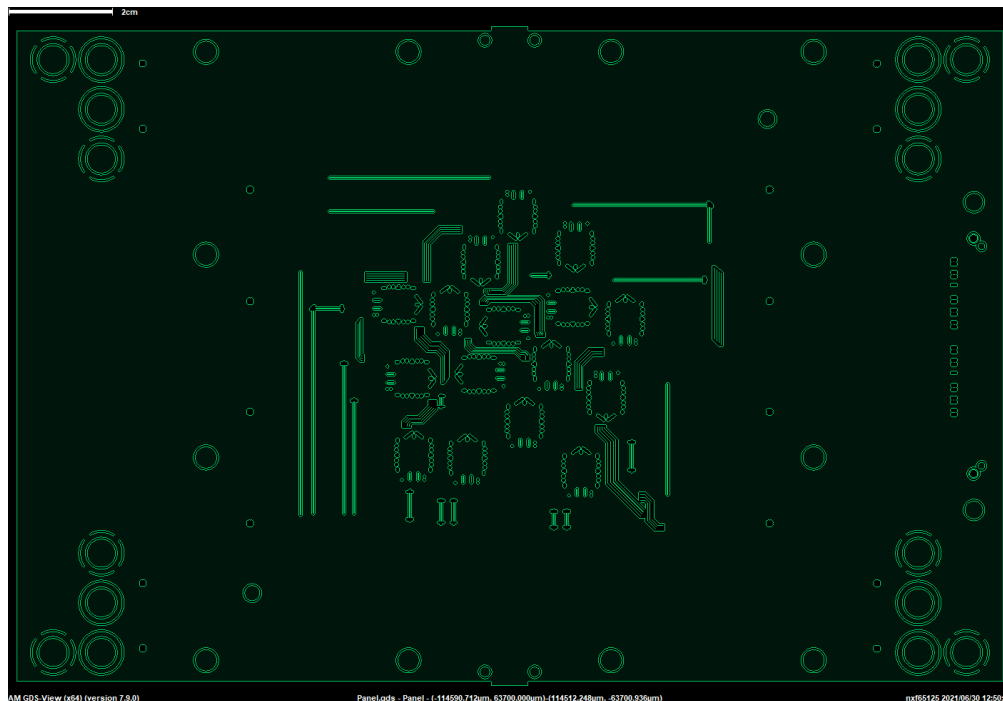


Figure A.2: Panel top view - Layer 2

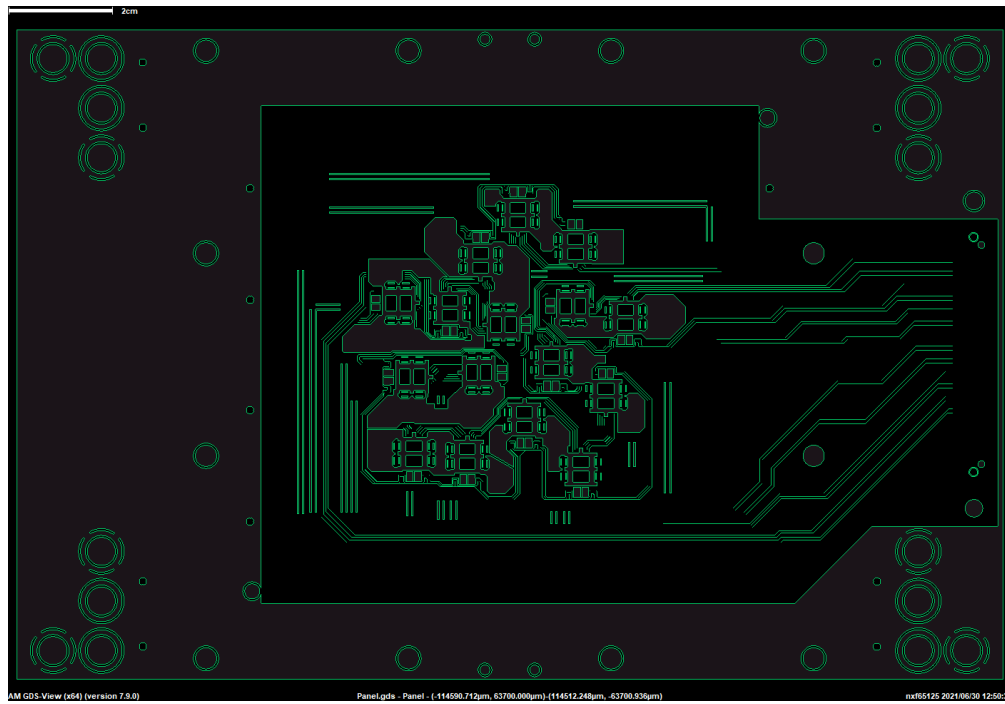


Figure A.3: Panel top view - Layer 3

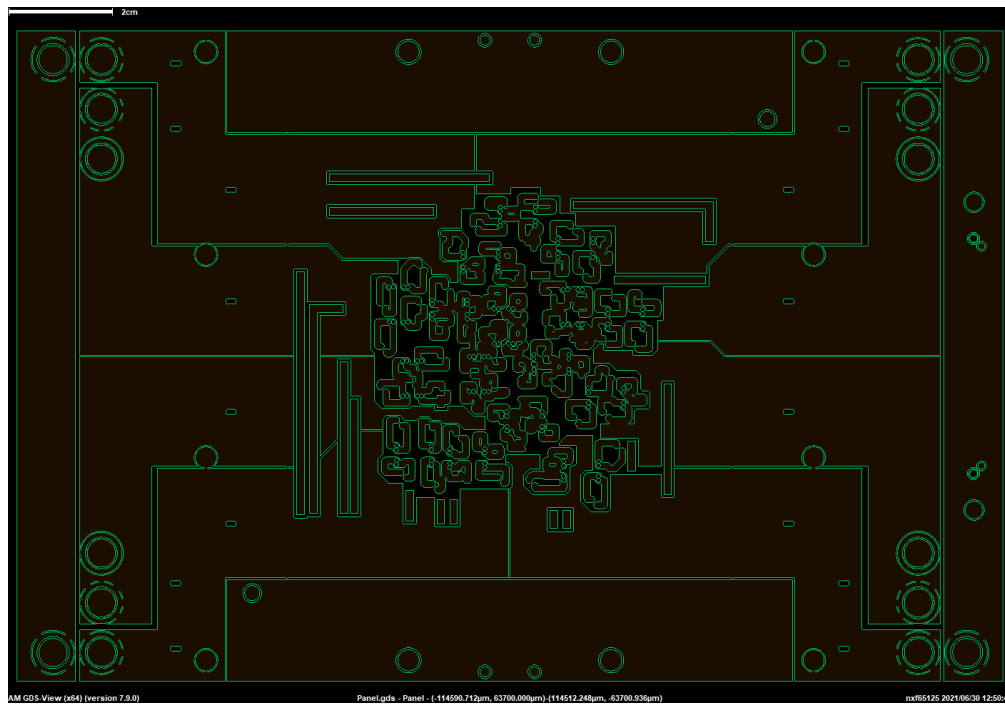


Figure A.4: Panel top view - Layer 4

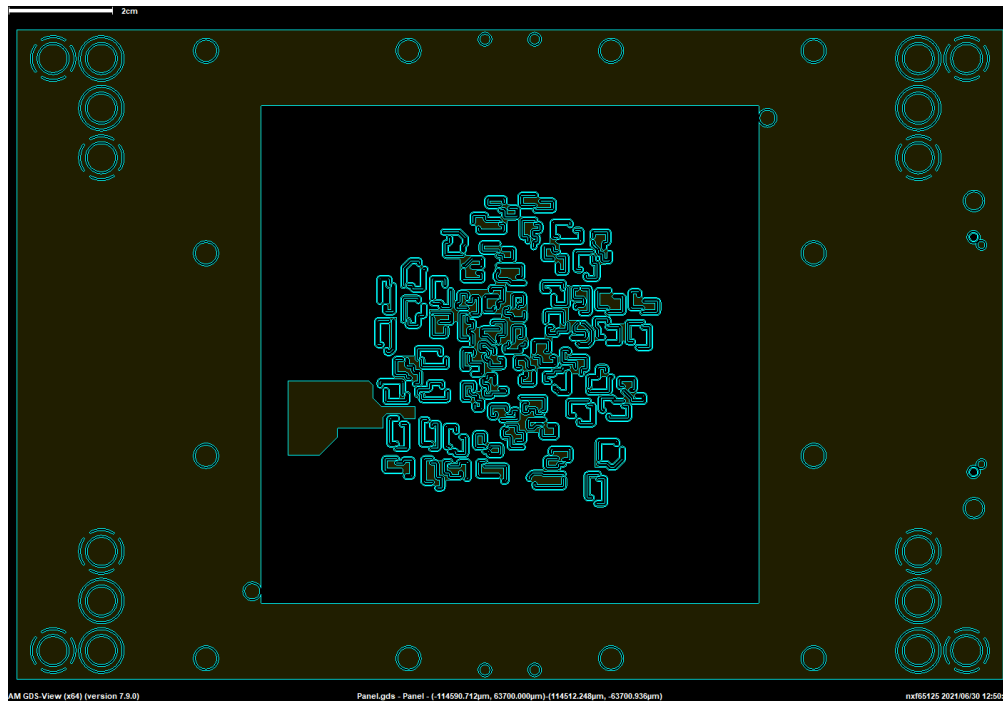


Figure A.5: Panel top view - Layer 5

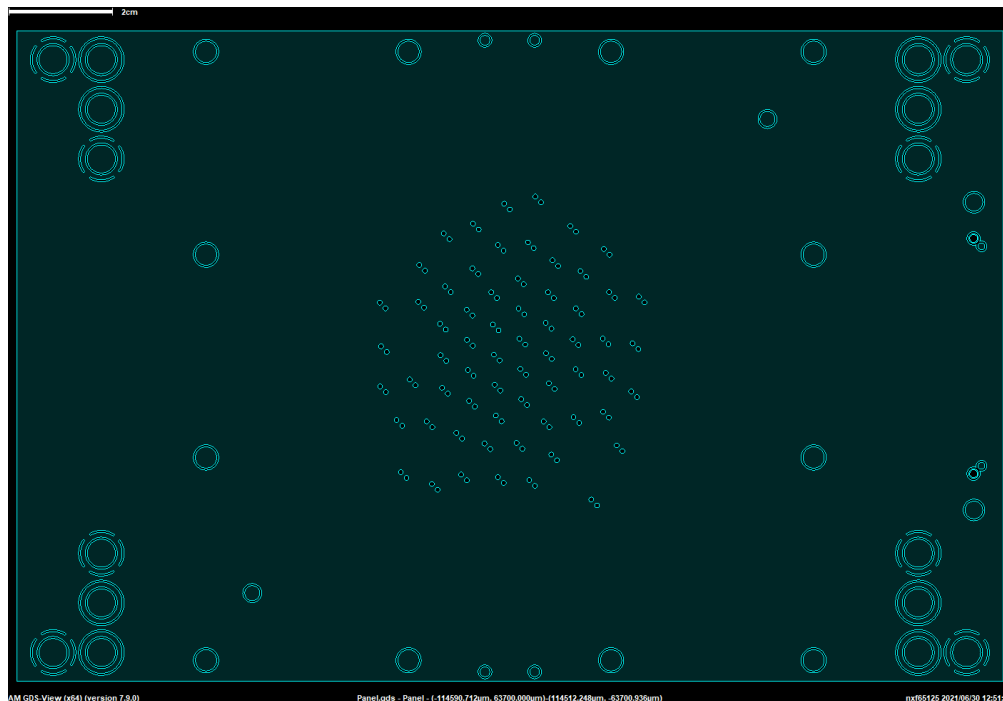


Figure A.6: Panel top view - Layer 6

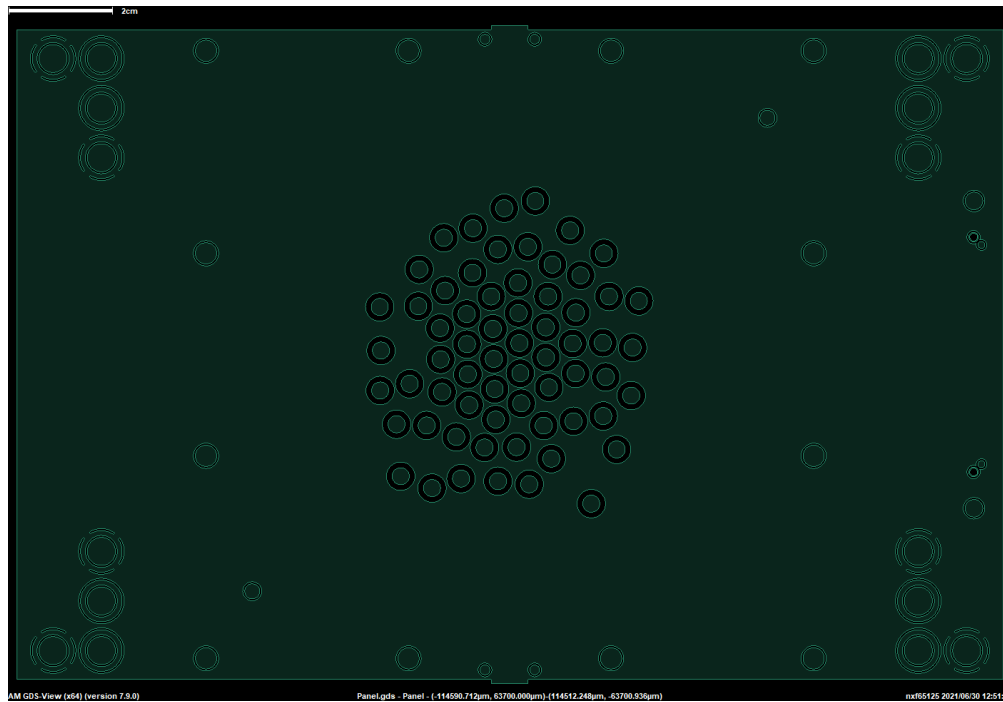


Figure A.7: Panel top view - Layer 7

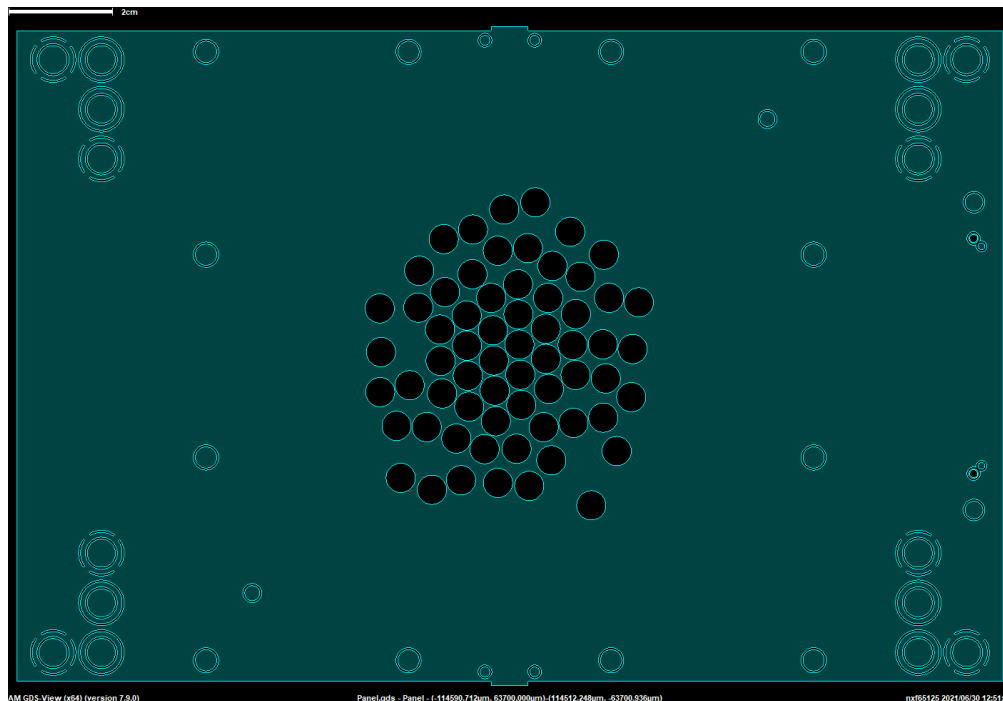


Figure A.8: Panel top view - Layer 8

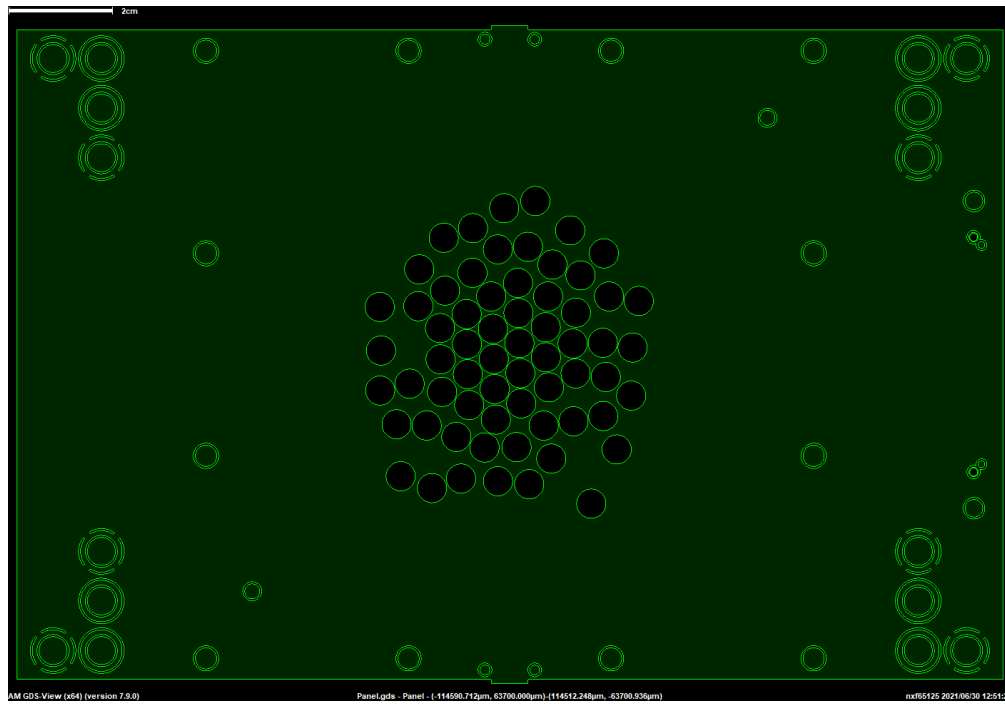


Figure A.9: Panel top view - Layer 9

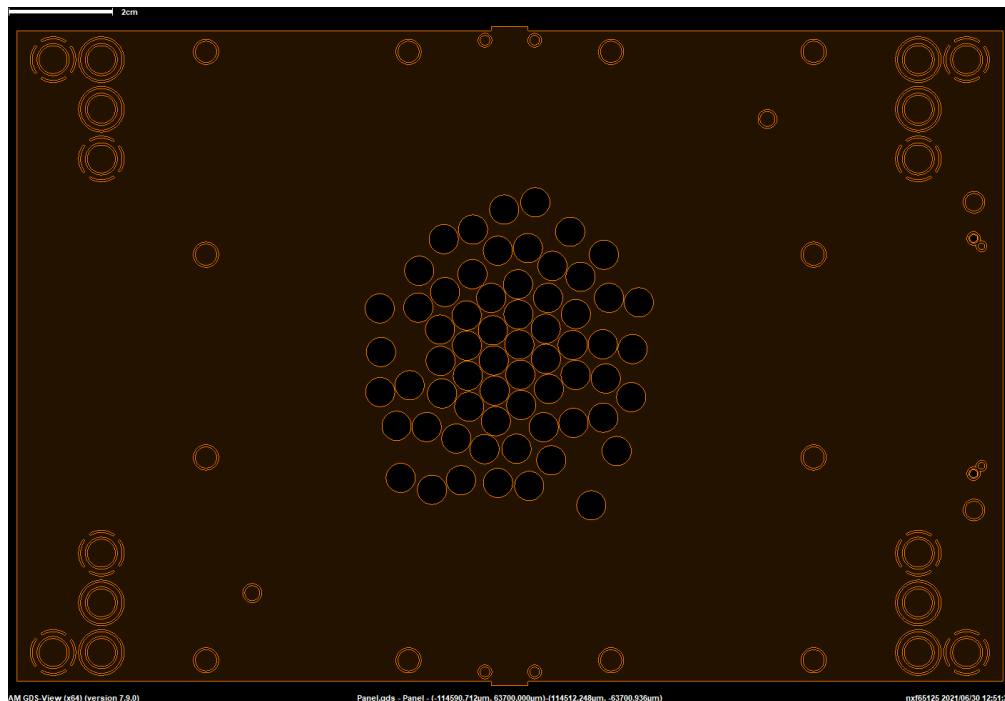


Figure A.10: Panel top view - Layer 10

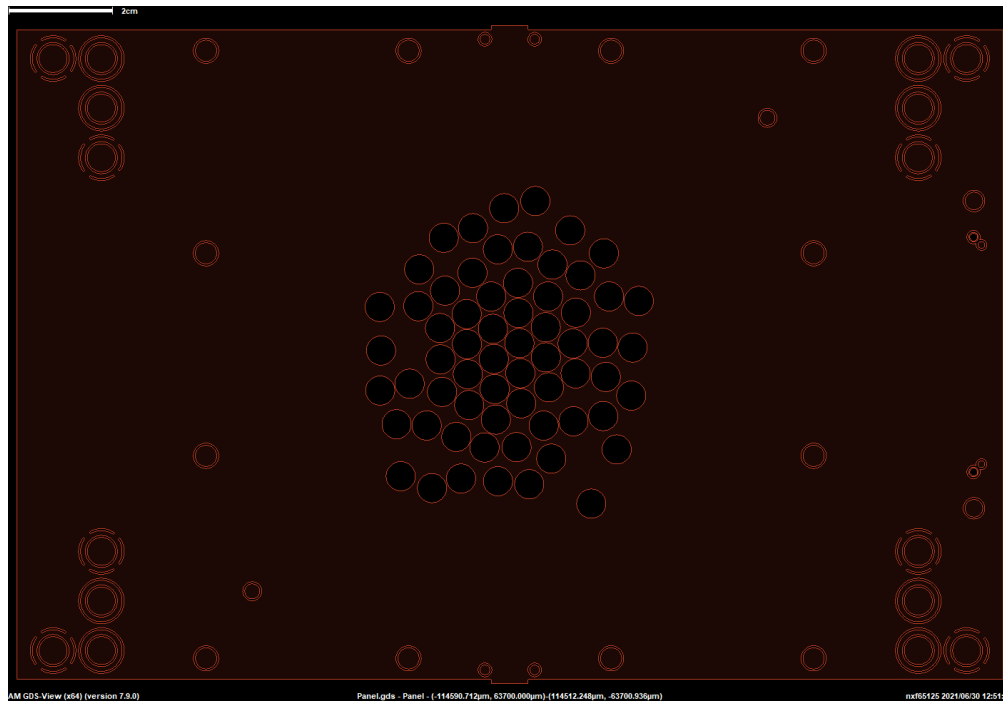


Figure A.11: Panel top view - Layer 11

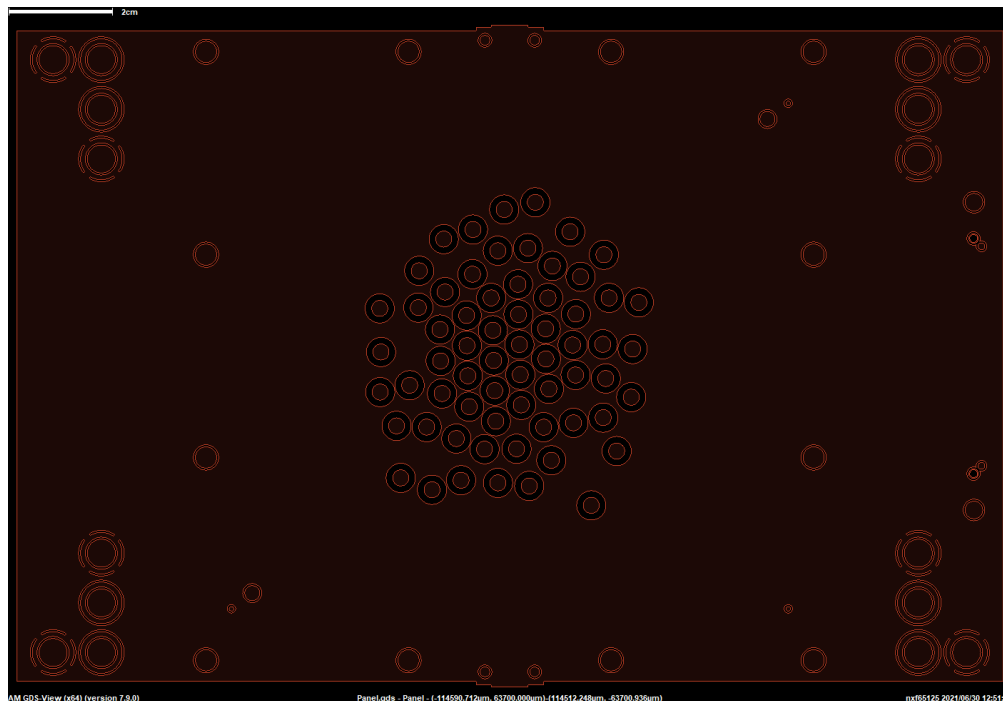


Figure A.12: Panel top view - Layer 12



## Appendix B

# Test board layout

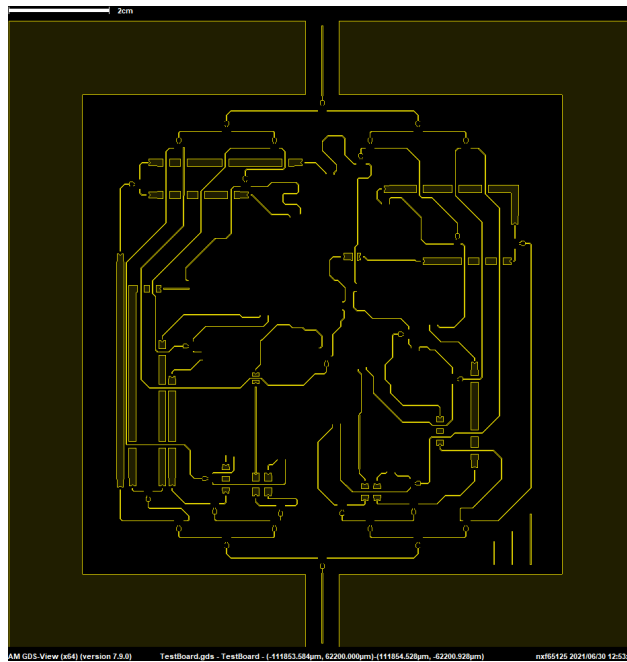


Figure B.1: Panel top view - Layer 1

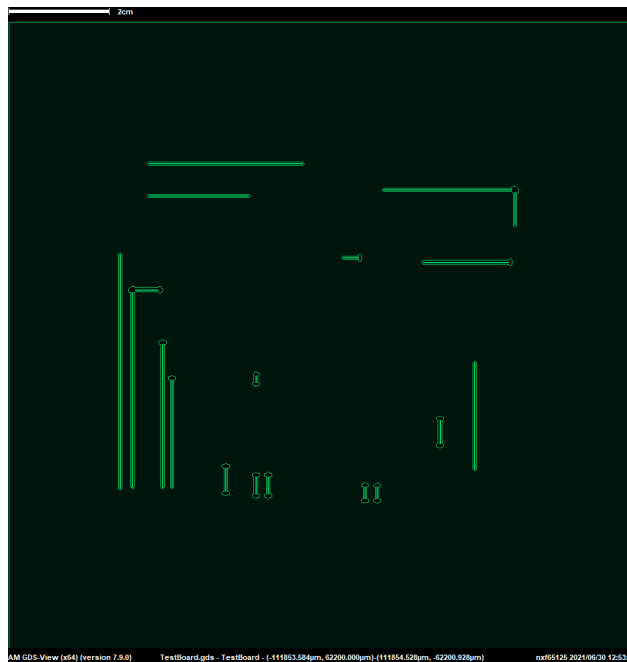


Figure B.2: Panel top view - Layer 2

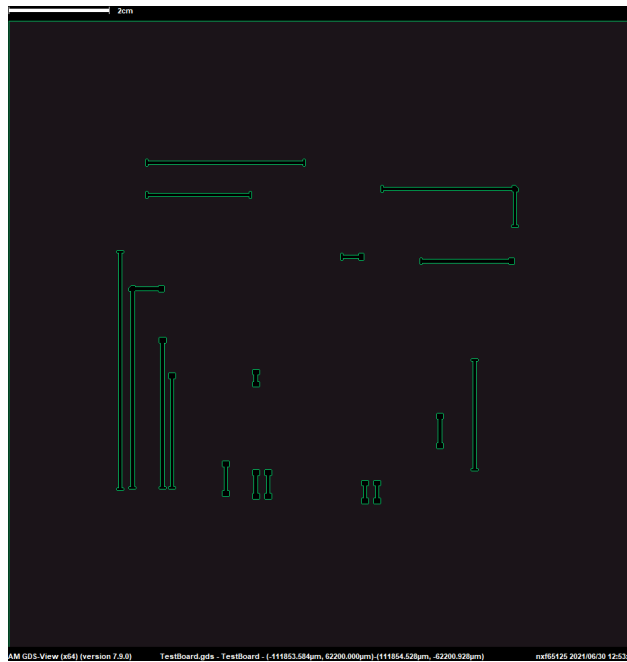


Figure B.3: Panel top view - Layer 3

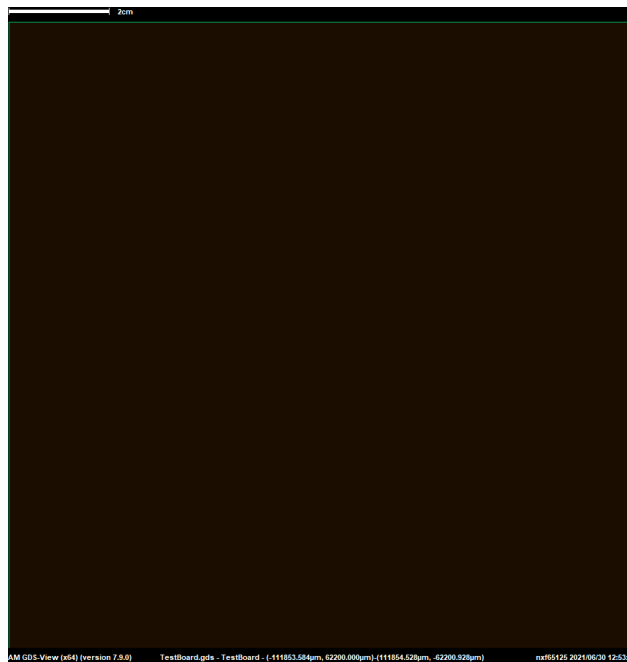


Figure B.4: Panel top view - Layer 4